공학박사 학위논문

# Fabrication of photoelectrodes with enhanced light utilization for dye-sensitized solar cells

염료감응형 태양전지를 위한

향상된 빛의 활용성을 가진 광전극 제조

2015년 2월

서울대학교 대학원

화학생물공학부

최 정 우

# Abstract

# Fabrication of photoelectrodes with enhanced light utilization for dye-sensitized solar cells

**Jung-Woo Choi**

**School of Chemical & Biological Engineering**

**Seoul National University**

An increase in global energy demand, environmental concerns and the finite nature of fossil fuels have led to a great interest and development in the field of renewable energy sources. Solar energy is one of the most promising renewable energy sources because of its cleanliness and abundance. Among photovoltaic devices, dye-sensitized solar cells (DSSCs) have attracted substantial attention as a renewable energy conversion device because of their low production cost, easy fabrication process, and aesthetically appealing design. However, in order for DSSCs to realistically

be considered an alternative to conventional solid-state photovoltaic devices, improvements in power conversion efficiency must be made. For improving the efficiency of DSSCs, the light absorption performance of photoanode, a key component of DSSCs, should be enhanced as much as possible to increase the production of photocurrent. Thus far, various attempts have been made to enhance the light harvesting efficiency of photoanodes. These efforts include developing new sensitizers with a broader range of absorption wavelength and a higher extinction coefficient, construction of new semiconducting electrode structures with light scattering properties, mixing different dyes for co-sensitization, and introducing non-radiative resonance energy transfer concepts. Nevertheless, it is still difficult to attain the desired level of light efficiency that would lead to significantly improved efficiency. In this study, new approaches for obtaining enhanced light utilization in photoanodes of DSSCs are demonstrated by incorporating optical-active inorganic materials such as quantum dots and precious metal nanoparticles into the photoanode of DSSCs.

The first part presents dye-sensitized solar cells with silica-coated quantum dot embedded nanoparticles ($SiO_2$/QD@$SiO_2$ NPs). QDs have

been considered promising materials with potential to be applied to photovoltaic devices owing to their powerful light absorption property. However, it is hard to apply QDs to DSSCs because of their instability in iodide pair electrolyte system which is most commonly used in DSSCs. To overcome this problem, QDs were embedded in $SiO_2$ nanoparticle and coated with thin $SiO_2$ layer. $SiO_2$/QD@$SiO_2$ NPs were incorporated into the photoanode of DSSCs. The enhanced performance of the $SiO_2$/QD@$SiO_2$ NP containing DSSC was believed to be mainly due to the improved short-circuit current density ($J_{SC}$), which was a direct result of enhanced light utilization in the photoanode. Rather than working as a sensitizer, QDs in DSSCs act as a light reservoir that absorb the extra light and re-emit the absorbed light.

The second part discusses plasmon-enhanced dye-sensitized solar cells using $SiO_2$ spheres decorated with tightly assembled silver nanoparticles (Ag NPs). The plasmonic enhancement effects of the photoanode in DSSCs were investigated. To activate the strong plasmon coupling, new structure of Ag NPs assembly was designed through electromagnetic wave simulation. Tightly assembled Ag NPs on a $SiO_2$ core showed broadband plasmonic

absorption developed by coupled plasmon modes, which was not limited to a specific wavelength. By incorporating $SiO_2$-t-Ag@$SiO_2$ into the photoanodes of DSSCs, light absorption by the photoanode thin films definitely increased and overall power conversion efficiencies of DSSCs were improved.

iv

# Contents

# List of Tables

# List of Figures

xv

# Chapter 1.  Introduction

## 1.1 Solar energy and solar cells

Energy is everywhere and drives everything. Our modern society has come to depend on its abundance, convenience, and potential. It is a motivating force that lights our world, drives our vehicles, warms or cools our dwellings. However, planet Earth is facing a serious energy crisis owing to an increase in global energy demand, continued dependence on fossil-based fuels for energy generation and transportation, and a rapid increase in world population. Global energy consumption is expected to rise by 41% from 2012 to 2035, and in 2050 the mean global energy consumption will be 28 TW.(The current world power consumption is ~15 TW.) Excessive burning of fossil fuels is not only depleting natural resources, but is resulting in an increase of carbon dioxide emissions, which scientists believe is responsible for increasing average global temperatures.[1]

To overcome this energy problem, many researchers have tried to commercialize many types of new & renewable energy sources which are naturally replenished such as sunlight, wind, rain, tides, waves and geothermal

heat.[2] Above all, solar energy has the largest potential to satisfy the future global need for renewable energy sources. From the $1.7 \times 10^5$ TW of solar energy that strikes the earth`s surface, a practical global solar potential value is estimated to be about 89,300 TW.[3]

Solar cells, also called photovoltaic (PV) cells, convert sunlight directly into electricity. PV gets its name from the process of converting light (photons) to electricity (voltage), which is called the PV effect. The PV effect was discovered in 1954, when scientists at Bell Telephone discovered that silicon created an electric charge when exposed to sunlight.[4]

Photovoltaics can be classified into so-called $1^{st}$, $2^{nd}$ and $3^{rd}$ generation. (Figure 1.1) The first generation PV is the oldest and the mostly common used technology type due to their high efficiencies, which is based on silicon wafers. Generally there are two types of the first generation solar cells. They differ by their crystallization levels. If the whole wafer is only one crystal, it is called monocrystalline solar cell. If wafer consist of crystal grains, it is called polycrystalline solar cell. Although power conversion efficiency of monocrystalline solar cells is higher than polycrystalline solar cells, production of polycrystal wafer is easier and cheaper. However, the first generation cells require expensive manufacturing technologies. Concepts consuming less material are based on thin-film technology and are considered

2

as the second generation photovoltaics. Despite of their lower efficiencies than the first generation solar cells, their costs are also less than silicon-based solar cells. These thin films can also be grown on flexible substrates. Therefore the second generation solar cells are applicable on textile products or on foldable devices. The second generation solar cells include amorphous Si (a-Si) based thin films solar cells, Cadmium Telluride/Cadmium Sulfide (CdTe/CdS) solar cells and Copper Indium Gallium Selenide (CIGS) solar cells.[5] Finally, the third generation photovoltaics aim at overcoming the so-called Shockley Queisser limit, which include organic solar cells and dye-sensitized solar cells (DSSCs). Their operation mechanism is not a traditional p-n junction but a photoelectrochemical reaction. The semiconductor nanomaterials and conducting polymers were used as elements of solar cells and fabrication process are relatively cheap because the expensive and high-vacuum processes needed for the traditional devices can be avoided.[6,7] However, they are still in the research phase due to the relatively low power conversion efficiency and low stability.
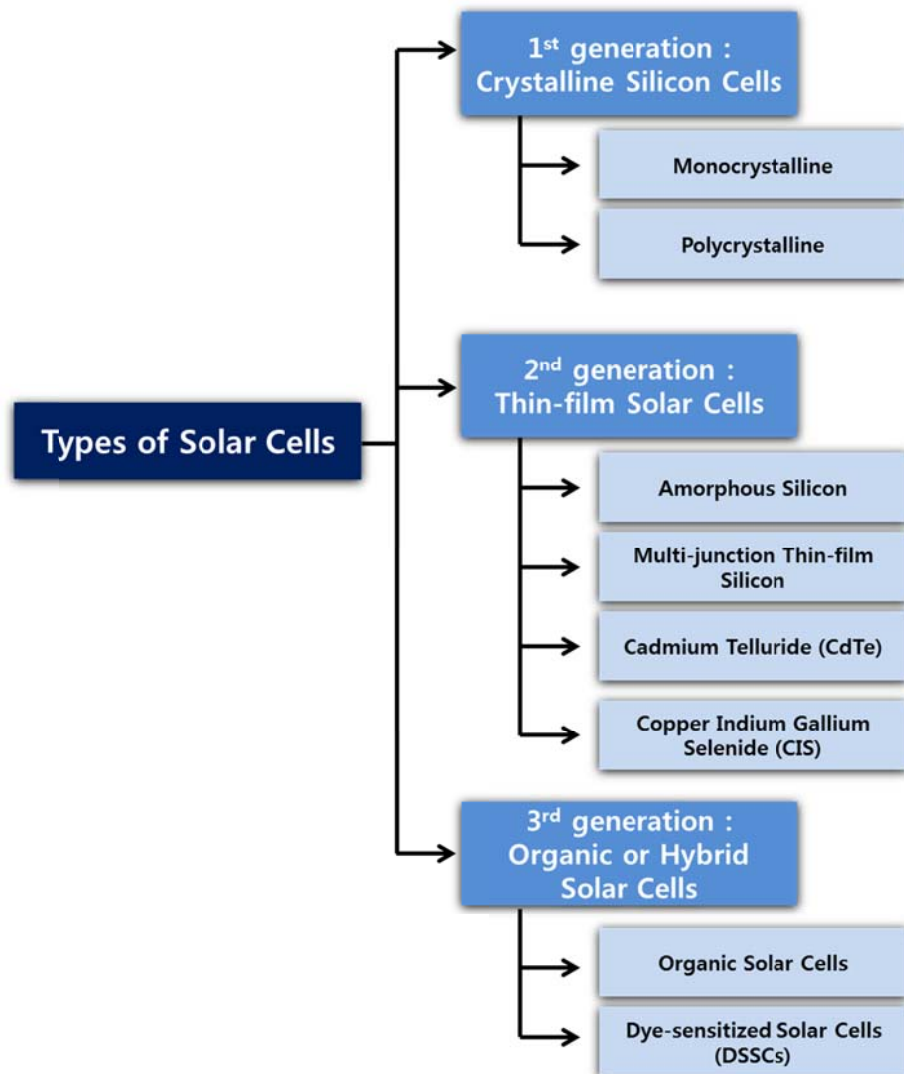
**Figure 1.1 Classification of solar cells**

## 1.2  Dye-sensitized solar cells (DSSCs)

Since 1991, following the demonstration of dye-sensitized solar cells (DSSCs) for the first time by M. Grätzel and B. O`Regan,[8] DSSCs have been attracting attention of both researchers and industries worldwide. Due to their low material cost, easy and inexpensive methods of fabrication, reasonably good power conversion efficiency and aesthetically appealing design, DSSCs are being considered to be a potential alternative to expensive conventional p-n junction solar cells. Furthermore, a dye used in dye-sensitized solar cells can absorb diffused sunlight and fluorescent light. DSSCs also work in cloudy weather and low-light conditions, while the other traditional cells would fail at illumination below an onset range. This makes them suitable for running small devices indoors. DSSCs also work at wider angles, a fact which makes the cells absorb most of the available sunlight. Besides, DSSCs are composed of light and mechanically robust materials that require no special protection. However, relatively low conversion efficiency and poor stability are major disadvantages of DSSCs.

### 1.2.1 Components and working principles of DSSC

Dye-sensitized solar cells (DSSCs) are a kind of photoelectrochemical cells, which operate differently from conventional p-n junction solar cells. A DSSC consists of a photoanode (photoelectrode), which is made up of a wide band gap semiconductor ($TiO_2$, $SnO_2$, $ZnO$, $Nb_2O_5$, etc.) with sensitizer dye molecules adsorbed on it, an electrolyte and a conductive substrate coated with a catalyst (Pt, carbon, etc.) as cathode.[9-11]

The wide band gap semiconductor is sensitized with the dye molecule that absorbs maximum in the visible range of the solar spectrum. The semiconductor nanoparticles provide a large surface area for adsorption of the dye, leading to absorption of sufficient amount of light by the photoanode. $TiO_2$ is turned out to the most versatile, delivering the highest efficiency. $TiO_2$ is chemically stable, non-toxic and readily available. Typically, the $TiO_2$ film thickness is ca. 10 $\mu$ m and the $TiO_2$ nanoparticle size 10-30 nm in diameter. The porosity is 50-60%. The porous semiconductor layer is made on a transparent conducting oxide (TCO) glass substrate, such as F-doped $SnO_2$ (FTO) glass, which is externally connected to the cathode. In general, the cathode is a TCO glass substrate with a catalyst such as Pt deposited.

The dye molecules commonly used in DSSCs are polypyridyl complexes of

ruthenium (Ru). Ru complexes have a broad absorption spectrum, suitable excited and ground state energy levels, relatively long excited-state lifetime, and good chemical stability. The N3 and N719 dyes, most famous Ru complexes, are considerable as reference dyes for DSSC and are used as a base for designing other dyes. However, the high cost and low earth abundance of noble metals has stimulated interest in organic dyes based on donor-linker-acceptor (DLA) structure.[12-14] Organic dyes typically have higher absorption coefficient, are considerably less costly, and are relatively easy to synthesize. However, dye aggregation and short lifetimes are the inherent problems of organic dyes.

Inorganic semiconductor quantum dots (QDs) are another promising materials as sensitizers because of their tunable size/shape-dependent energy band gaps, high optical absorption coefficients, large dipole moments, and multiple exciton generation characteristic.[15,16] The most commonly used quantum dot sensitizers can be generally classified into three types: (a) cadmium-chalcogenide QDs, including CdS, CdSe, and CdTe, (b) lead-chalcogenide QDs, including PbS, PbSe, (c) antimony sulfide $Sb_2S_3$ QDs.

Recently, halide perovskite $CH_3NH_3PbX_3$ (X = Cl, Br, or I) sensitizers have attracted attention because of their excellent light harvesting properties. In 2009, the first perovskite-sensitized solar cell was reported, showing power

conversion efficiency (PCE) of 3.81% for $CH_3NH_3PbX_3$.[17] Early in 2014, PCE of perovskite $CH_3NH_3PbX_3$-based solar cells was further lifted to 16.7%.[18]

Iodide and triiodide (i.e. $I^- /I_3^-$) redox couple in solvent is a popular liquid electrolyte used in DSSCs because of its satisfactory kinetic properties, such as fast oxidation of $I^-$ at the photoanode/electrolyte interface for efficient dye regeneration and slow reduction of $I_3^-$ at the electrolyte/counter electrode interface for high carrier collection, excellent infiltration, relative high stability, low cost and easy preparation.[19] However, several disadvantages exist for the $I^-/I_3^-$ electrolyte. Disadvantages such as the absorption of visible light at 430 nm, corrosion of the precious metal counter electrode (for example, Pt, Au), and an upper limit on $V_{OC}$ of 0.9 V, significantly restrict further development of DSSCs using this electrolyte system.[20] As a result, several alternative electrolytes have been investigated, including $Co^{(II/III)}$ polypyridyl complex, ferrocenium/ferrocene ($Fc/Fc^+$) couple, $Cu^{(I/II)}$ complex, and thiolate/disulfide mediator.[19]

On illumination, the dye molecule absorbs photons of wavelength corresponding to the energy difference between its highest occupied molecular orbital (HOMO) and lowest unoccupied molecular orbital (LUMO). Electrons from the ground state of the dye (S) are now promoted to excited

state (S*), known as photoexcitation of dye. This electron in the excited state of the dye is then injected into conduction band (CB) of $TiO_2$. The electrons after being injected into CB of $TiO_2$ are transported through the semiconductor layer by diffusion to reach the conducting layer. The iodide ion donates electron to the oxidized dye $(S^+)$ at photoanode surface and regenerates the dye molecule. The oxidized species of the electrolyte is reduced to iodide at the cathode. The above processes go in cycle, and consequently currents flow through the external circuit as long as light is incident on the cell.(Figure 1.2) Besides the above processes, several recombination reactions can take place at different interfaces in the cell and thereby reduce performance of the cell. The two important recombination reactions, which have been considered to be important, are recombination of $TiO_2$ CB electron and electron from the FTO with triiodide ion in the electrolyte. However, these recombination processes occur at a slow rate and thus, the processes required to take place for working of the cell are kinetically favored. The recombination at the $TiO_2$/electrolyte interface has to be slower than diffusion of electron through the $TiO_2$ film for working of the cell at all. Since injection of electron into CB of $TiO_2$ from the excited dye is an ultra-fast process and takes place in picoseconds, electron transport through the $TiO_2$ film determines the current collection efficiency. Higher

crystallinity and improved connectivity between the particles cause faster diffusion of electron through the photoanode, which results in higher current density in the cell.

**Cell reactions**

$$S_{(adsorbed)} + h\nu \rightarrow S^*_{(adsorbed)}$$

$$S^*_{(adsorbed)} \rightarrow S^+_{(adsorbed)} + e^-_{(injected)}$$

$$S^+_{(adsorbed)} + A^- \rightarrow S_{(adsorbed)} + A$$

$$A + e^-_{(counter\ electrode)} \rightarrow A^-$$
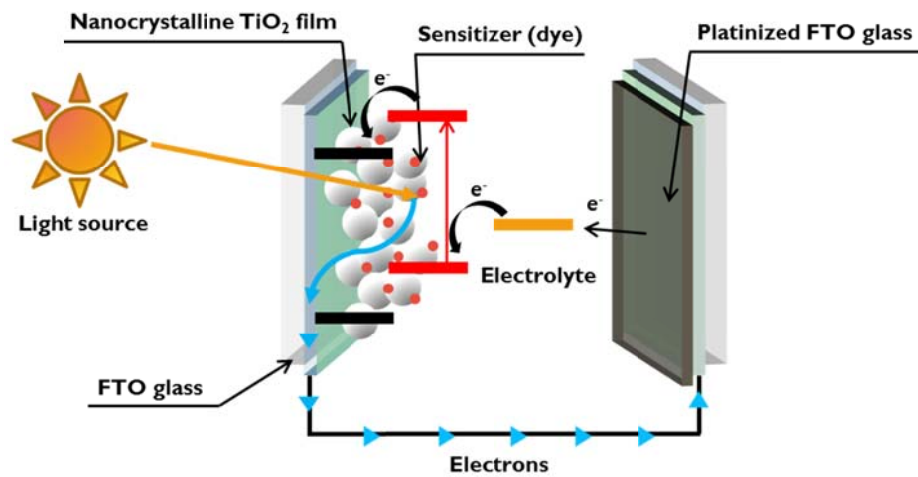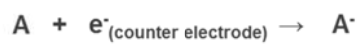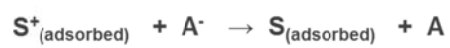
**Figure 1.2 The structure and operational principles of DSSC.**

### 1.2.2 Characterization techniques

In order to understand DSSC and the complex interaction of its components, it is needed to study the complete cell, besides the investigations of the separate components. Because DSSC is an electrochemical devices which is completely different from the classical p-n junction cell, electrochemical analysis is useful to characterize the components of DSSC.[21]

### 1.2.2.1 The current-voltage (*I-V*) characteristics

The current-voltage (*I-V*) characteristics of a solar cell under illumination are used to determine the power conversion efficiency, $\eta$. (Figure 1.3) Because DSSCs have a relatively slow electrical response due to their high interfacial capacity, the voltage scan should be sufficiently slow to avoid errors in the current measurement. From the *I-V* curve, the short-circuit current, $I_{SC}$ (or short-circuit current density: $J_{SC}$), is determined at the $V = 0$ V intercept, while the open-circuit potential, $V_{OC}$, is found at $I = 0$ intercept. The maximum output power of the solar cell is found where the product $I \times V$ reaches a maximum.

$$\eta = \frac{|JV|_{max}}{P_{in}} = \frac{J_{sc}V_{OC}ff}{P_{in}}$$

$$\text{Fill factor } (ff) = \frac{J_{max} \times V_{max}}{J_{sc} \times V_{OC}}$$

The power conversion efficiency ($\eta$) is given by where $P_{in}$ is the power density of the incident light and *ff* is the fill factor. It is common practice to use white light from a solar simulator as the light source for efficiency measurements. The standard irradiance spectrum for the solar cell measurements is AM 1.5 G. This condition means that the angle of elevation of the sum is $42°$. The solar spectrum of AM 1.5 G is shown in Figure 1.4. In the figure, the maximum current (short-circuit current) for solar cells converting all incident photons below the absorption onset wavelength into electric current is shown. For example, the maximum short-circuit current for a solar cell with and absorption onset of 700 nm is 20 mA/cm$^2$.
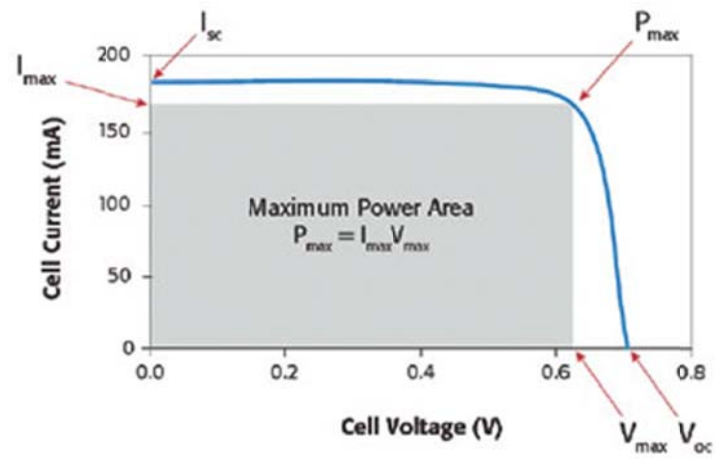
**Figure 1.3** *I-V* **characteristics of solar cell.**

**(ref. http://www.keithley.com/solar_cell)**
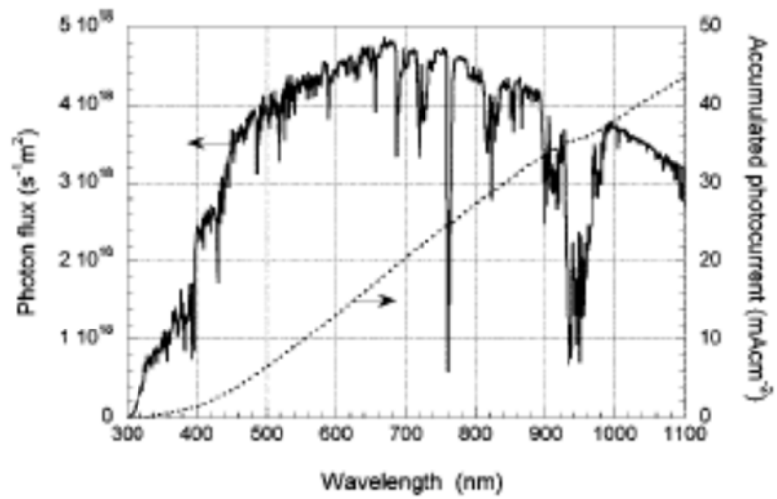
**Figure 1.4 Photon flux of the AM 1.5 G spectrum at 1000 W m$^{-2}$ (ASTM G173-03), and calculated accumulated photocurrent. (ref. 11)**

**1.2.2.2 Incident photon-to-current conversion efficiency (IPCE) and absorbed photon-to-current conversion efficiency (APCE)**

The spectral response of dye-sensitized solar cells is determined by measuring the incident photon-to-current conversion efficiency (IPCE). It is measure of how efficiently the cell converts the incident light into electrical energy at a given wavelength. The principle of IPCE is based on illuminating the sample by a monochromatic light and recording the device electrical current. By varying the frequency of the light the entire curve of the current as a function of wavelength can then be established. The IPCE can be expressed as follows:

$$IPCE(\lambda) = LHE(\lambda)\varphi_{inj}(\lambda)\varphi_{reg}\eta_{CC}(\lambda)$$

Where LHE is the light-harvesting efficiency, $\varphi_{inj}$ and $\varphi_{reg}$ are the quantum yields for electron injection and dye regeneration, respectively, and $\eta_{CC}$ is the charge collection efficiency.

The absorbed photon-to-current conversion efficiency (APCE) shows how efficient the numbers of absorbed photons are converted into currents. APCE

is obtained by dividing the IPCE value by the light harvesting efficiency (LHE).

### 1.2.3   Light utilization in photoanode

The power conversion efficiency of DSSCs needs to be improved further in order for DSSCs to become an economically feasible alternative to conventional photovoltaic devices. Research efforts have been focused on the improvement of the sensitized photoanode, dye, electrolyte, cathode and their interfaces, as well as the fabrication technologies.

For improving the efficiency of DSSCs, the light absorption performance of photoanode—a key component of DSSCs—should be enhanced as much as possible to increase the production of photocurrent. It is estimated that a power conversion efficiency over 15% using $I^-$ /$I_3^-$ as redox couple would require a photoanode absorbing 80% of sunlight from 350 to 900 nm. To date, the most efficient conventional sensitizers are polypyridyl ruthenium dyes with a bandgap of about 1.8 eV, *e.g.*, N3 and N719.[22,23] Their strong absorption peaks at 530 nm are observed while the absorption coefficient drastically decreases at longer wavelength.(Figure 1.5) Therefore, various attempts have been made to enhance the light harvesting efficiency of

photoanode without sacrificing the overall performance. These efforts include synthesizing new sensitizers with a broader range of absorption wavelength and a higher extinction coefficient,[24-27] designing new semiconducting electrode structures with light scattering properties,[28-32] mixing different dyes for co-sensitization,[33,34] and introducing non-radiative resonance energy transfer concepts.[35-38] Nevertheless, it is still difficult to attain the desired level of light efficiency that includes improved efficiency throughout the whole visible light region.
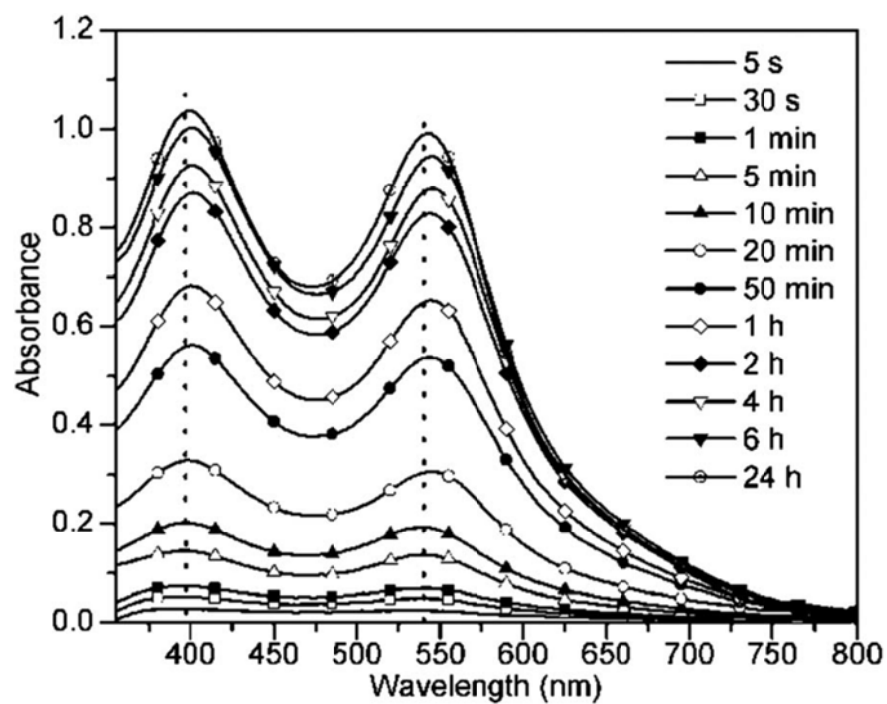
**Figure 1.5 UV-Vis spectra of N719-coated TiO₂ films after different dye**

**dipping times (from 5 s to 24 h). (ref 22)**

## 1.3 Objectives of this dissertation

As discussed previous sections, the power conversion efficiency of dye-sensitized solar cells (DSSCs) needs to be further improved for them to be used as an economically viable alternative to conventional photovoltaic devices. Among the components of DSSC, the key element which greatly influences the overall cell performance is the photoanode which absorbs the incident light and generates photoelectrons. In this study, new approaches for obtaining enhanced light utilization in the photoanode of DSSCs are demonstrated by incorporating optical-active inorganic materials, such as quantum dots and metal nanoparticle, into photoanodes of DSSCs.

The main dissertation consists of two parts. The first part (Chapter 2.) presents dye-sensitized solar cells with silica-coated quantum dot (QD) embedded nanoparticles. To overcome the instability of QDs in iodide pair electrolyte system, QDs were embedded in $SiO_2$ nanoparticle and coated with thin $SiO_2$ layer. Silica-coated QDs on photoanodes fluoresced brightly when stimulated with visible wavelength laser. Moreover, confocal laser scanning microscopy (CLSM) revealed that the narrow emission of QDs was evenly distributed over a wide area. Reduction of fluorescence after dye-adsorption indicated that the photoanode absorbed the re-emitted light from QDs. By

incorporating QDs into the photoanode, UV-vis absorption was considerably increased, which positively affected the cell performance. QDs in DSSCs did not work as sensitizers but as light reservoir that absorb the extra light and re-emit the absorbed light.

The second part (Chapter 3.) discusses plasmon-enhanced dye-sensitized solar cells using $SiO_2$ spheres decorated with tightly assembled silver nanoparticles (Ag NPs). The plasmonic enhancement effects of a photoanode in DSSCs were investigated. Conventionally, surface plasmon resonance (SPR) can enhance light utilization in photovoltaic devices by the excitation of localized surface plamons (near-field) and by light scattering from metal nanoparticles (far-field). In addition, new structure of Ag NPs assembly was designed through electromagnetic wave simulation to activate the strong plasmon coupling. Tightly assembled Ag NPs on a $SiO_2$ core showed broadband plasmonic absorption developed by coupled plasmon modes, which was not limited to a specific wavelength. By incorporating $SiO_2$-t-Ag@$SiO_2$ into the photoanodes of DSSCs, light absorption by the photoanode thin films definitely increased and overall power conversion efficiencies of DSSCs were improved.

**Figure 1.6 Schematic illustration of objectives of this dissertation.**

# Chapter 2. Dye-sensitized solar cells with silica-coated quantum dot

## 2.1 Introduction

Quantum dots (QDs) are semiconductor nanostructures that are small enough to exhibit quantum mechanical properties. Since the first directed synthesis of QDs, they have been applied to light emitting diodes (LEDs),[39] solar cells,[40,41] photoconductors,[42,43] field-effect transistor,[44,45] bio-labelling techniques and biosensors,[46] because of their notable characteristics including band gap tunability, broad extinction spectra, narrow emission spectra, excellent photostability, high extinction coefficient and multiple exciton generation property.

Over the last few years, QDs are considered promising materials with potential to be applied to photovoltaic devices owing to their powerful light absorption property. In most photovoltaics research, QDs have been used as sensitizer or co-sensitizer.[47,48] Quantum dot solar cells (QDSCs) are representative case, which have emerged as a viable alternative to other third-generation solar cells. However the overall efficiency of this cell is still low

compared to other types. The first problem arises with sensitizing QD materials replacing dyes in the system. It needs hole transporting materials like liquid or solid state electrolytes to regenerate oxidized sensitizers as well as to collect the electrons at the surface of counter electrode. Iodide pair electrolyte system which is commonly used in DSSC is corrosive to the quantum dot sensitizer. Therefore, alternative electrolyte that contains polysulfide proved to be a fairly good hole transporting material. A new problem arises due to low catalytic activity of Pt counter electrode with polysulfide electrolyte. Low catalytic activity has the undesired effect of high internal series resistance. The other problem arises from the deposition method. For the CdS deposition via successive ionic layered absorption and reaction (SILAR) method, only around 20% of the $TiO_2$ surface is covered. Lee and Lo reported that QDs are used as co-sensitizers to improve the power conversion efficiency of DSSCs.[49] However, because of poor chemical stability, a considerable decrease in the quantum yield of QDs is observed in corrosive iodide/triiodide-based electrolytes, thereby making it difficult to utilize QDs in conventional DSSCs.[50,51]

The encapsulation of QDs using silica has many advantages including water compatibility, facile chemical modification, low cytotoxicity, and excellent chemical stability.[52-54] Thus far, many studies for the development of

24

silica-encapsulated QDs have been published. They employ single QDs for encapsulation with the goal of obtaining a high quantum yield. However, the quantum yield of QDs dramatically decreases upon coating with silica. In this work, a number of QDs were embedded in one silica backbone to prepare chemically stable silica-coated QDs without any loss in quantum yield. As a result, these multiple-QD-containing NPs are brighter than single QDs, enabling an easier handling because of their bigger size (120 nm).

In this study, we immobilized silica-coated quantum dot-embedded silica nanoparticles ($SiO_2/QD@SiO_2$ NPs) on photoanodes of DSSCs and demonstrated that these $SiO_2/QD@SiO_2$ NPs were stable and enhanced the efficiency of the DSSC by enhancing the light utilization. (Figure 2.1) The $SiO_2/QD@SiO_2$ DSSC was analyzed using UV-vis spectroscopy, confocal laser scanning microscopy (CLSM), and incident-photon-to-current efficiency (IPCE) to verify the function of $SiO_2/QD@SiO_2$ NPs.
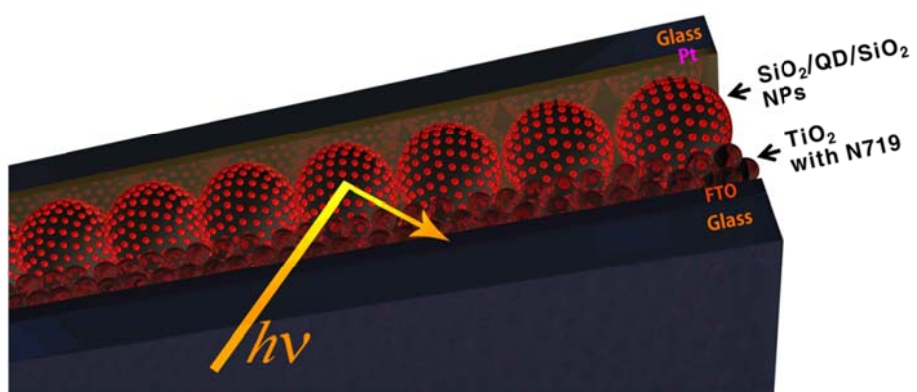
**Figure 2.1 Schematic illustration of dye-sensitized solar cell with silica-coated quantum dot embedded nanoparticles.**

## 2.2 Experimental section

### 2.2.1 Preparation of silica-coated quantum dot-embedded silica nanoparticles (SiO$_2$/QD@SiO$_2$ NPs)

Silica-core nanoparticles were prepared by the established method.[55] A 3 mL aliquot of ammonium hydroxide (NH$_4$OH) was added to 40 mL of ethanol containing 1.6 mL of tetraethyl orthosilicate (TEOS) under continuous vigorous magnetic stirring at 25 °C for 20 h. The SiO$_2$ spheres were centrifuged and washed with ethanol five times.

The prepared SiO$_2$ spheres were thiol-functionalized using 3-mercaptopropyltrimethoxysilane (MPTS). A 300 mg sample of SiO$_2$ spheres was dispersed in 6 mL of ethanol containing 60 mL of MPTS and 150 mL of NH$_4$OH. The solution was stirred at 25 °C for 12 h. The resulting MPTS-treated SiO$_2$ spheres were centrifuged and washed with ethanol three times. A 100 mg sample of the MPTS-treated SiO$_2$ NPs was then dispersed in 2 mL of ethanol, which was subsequently added to a solution of 100 mg of QDs (Nanosquare Inc., emission: 610 nm, core−shell type: CdSe−ZnS) dissolved in 0.5 mL of CHCl$_3$. After shaking for 5 min, 20 mL of CHCl$_3$, 1 mL of MPTS, and 1 mL of NH$_4$OH were added to the solution. After further shaking for 1 h,

the resulting solution was centrifuged and washed with ethanol five times. The collected powder residue was then dispersed in another solution containing 40 mL of ethanol, 1 mL of TEOS, and 1 mL of $NH_4OH$. The resultant solution was then shaken one final time for 12 h, after which it was centrifuged and washed with ethanol five times. Then, the prepared $SiO_2/QD@SiO_2$ NPs were re-dispersed in ethanol.

## 2.2.2 Preparation of photoanodes with $SiO_2/QD@SiO_2$ NPs

F-doped $SnO_2$ (FTO) glass plates (8 $\Omega/cm^2$, Pilkington TEC glass$^{TM}$) were cleaned in detergent solution using an ultrasonic bath for 20 min and washed with tap water and ethanol. The photoanodes composed of nanocrystalline $TiO_2$ were prepared using a previously reported procedure.[11] A paste composed of 20 nm anatase $TiO_2$ particles (Dyesol, DSL 18NR-T) for the transparent nanocrystalline layer was coated on the titanium tetrachloride ($TiCl_4$, 40 mM) treated FTO glass plates by Doctor blade method and then annealed under a programmed flow: at 325 °C for 5 min, at 375 °C for 5 min, at 450 °C for 15 min and finally 500 °C for 15min. A sample of $SiO_2$-$QD@SiO_2$ NPs dispersed in ethanol was introduced onto the prepared $TiO_2$ layer using a spin coater at room temperature and annealed at 200 °C for 30

28

min. The modified electrode was immersed into N719 dye solution (0.5 mM, N719 dissolved in a mixture of acetonitrile and $t$-butyl alcohol, v/v = 50:50) and kept at room temperature for 24 h. Then dyed electrode was washed with ethanol.

### 2.2.3 Fabrication of SiO$_2$/QD@SiO$_2$ DSSCs

A drop of 10 mM H$_2$PtCl$_6$ in 2-propanol was spread on FTO glass plate by spin coating followed by heating to 400 °C for 15 min. The prepared photoanode was assembled with Pt counter electrode into sandwich-type cell using thermal adhesive film (Surlyn: 60 μm, Dupont). The electrolyte solution was prepared by mixing 0.60 M 1-butyl-3-methylimidazolium iodide, 0.03 M I$_2$, 0.10 M guanidinium thiocyanate and 4-tert-butylpyridine in a mixture of acetonitrile and valeronitrile (v/v, 85:15). Before the measurement of photovoltaic performance, a mask of 0.16 cm$^2$ was attached.

### 2.2.4 Instruments

UV-vis absorption and reflectance spectra of the photoanodes were collected by UV-vis spectrometer (Jasco, V-670) with integrated sphere. A TEM images

were obtained using EF-TEM (Carl Zeiss, LIBRA 120). The photovoltaic performance was measured using a 500 W xenon lamp (XIL model 05A50KS source measure units and an AM 1.5 filter) at a power of 100 mW/cm$^2$. The incident photon-to-current efficiency was measured using solar cell quantum efficiency measurement system (QEX7, PV measurements, Inc.). Photoluminescence of deposited SiO$_2$-QD@SiO$_2$ was confirmed by confocal laser scanning microscope (Carl Zeiss LSM710).

## 2.3 Results and discussion

### 2.3.1 Preparation of silica-coated quantum dot-embedded silica nanoparticles (SiO$_2$/QD@SiO$_2$ NPs)

Silica-core nanoparticles (SiO$_2$ NPs) were synthesized by the Stöber method, the diameter of the silica-core NPs was approximately 120 nm. (Figure 2.2 (a)) Thiol groups were introduced on the surface of SiO$_2$ NPs by using mercaptopropyl trimethoxysilane (MPTS) as an organosilane coupling agent. QDs (Figure 2.2 (b)) were embedded on the surface of SiO$_2$ NPs, a carrier template. CdSe@ZnS was selected as a model quantum dot. CdSe has fair good bandgap that covers visible light region. Moreover, its emission wavelength can be easily tuned by size control. For high quantum yield, ZnS was coated on CdSe, which passivates surface nonradiative recombination sites.

Then, they were encapsulated in a silica shell for electronically and chemically insulating QDs. Figure 2.3 show transmission electron microscopy (TEM) images of silica-coated quantum dot-embedded silica nanoparticles (SiO$_2$/QD@SiO$_2$ NPs) They exhibit a core-shell structure and consist of 6 nm QDs (maximum emission at 610 nm) immobilized on a SiO$_2$ NPs core and a

SiO$_2$ shell. About ~5-nm-thick amorphous SiO$_2$ shell provide chemical stability to the QDs in an iodide/triiodide-based electrolyte. (Figure 2.3 (c,d)) The number of QDs on the silica core was estimated to be $\approx$200~300 per single silica NP. The resulting SiO$_2$/QD@SiO$_2$ NPs showed quantum yields of 64%.
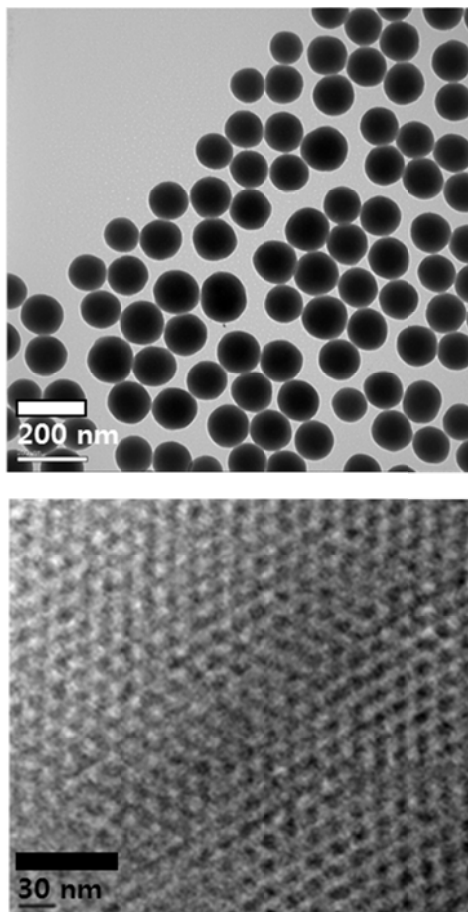
**Figure 2.2 TEM images of (a) silica nanoparticle (SiO$_2$ NPs), (b) quantum dots (emission: 610 nm, core–shell type: CdSe–ZnS).**
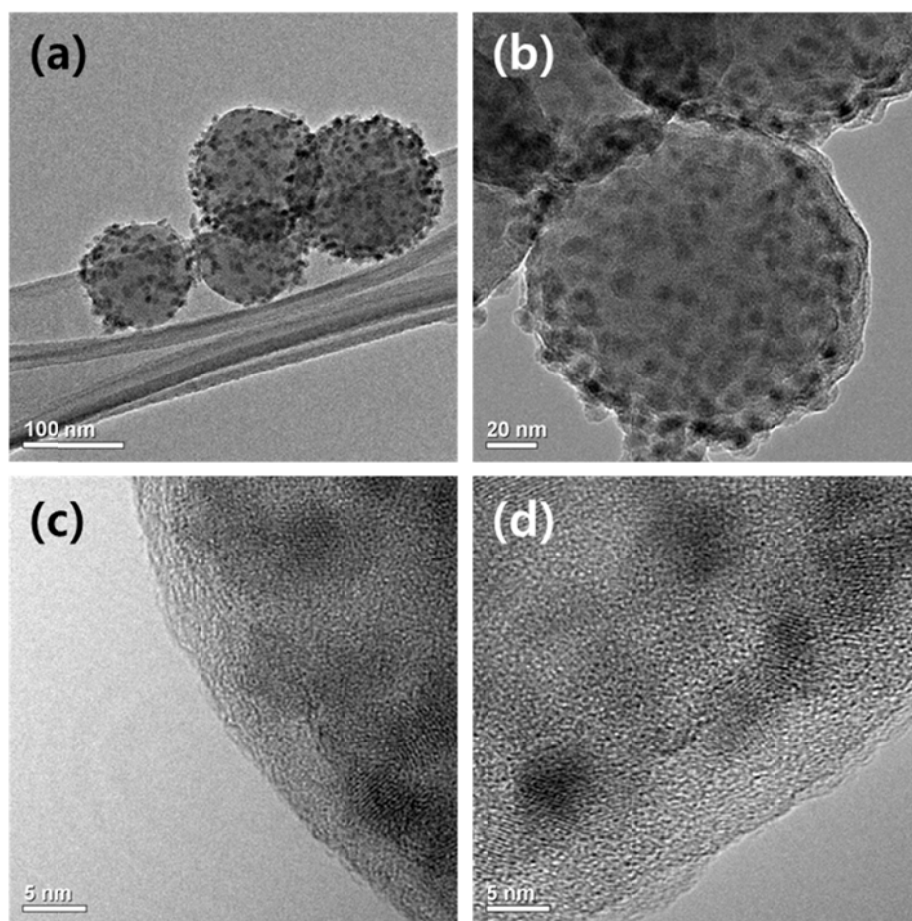
**Figure 2.3 TEM images of silica-coated quantum dot-embedded silica nanoparticles (SiO$_2$/QD@SiO$_2$ NPs).**

### 2.3.2 UV-vis spectra of modified photoanode

On $TiO_2$ thin film of the photoanode, $SiO_2$/QD@$SiO_2$ NPs that have great light absorption ability were introduced as light harvesting layer by spin coating. Because a part of incident light cannot be absorbed in dyed-thin film completely, $SiO_2$/QD@$SiO_2$ NPs are expected to hold unabsorbed light. To confirm the light utilization in modified photoanode, the optical properties were analyzed.

The UV-vis absorption spectra of photoanodes are shown in Figure 2.4. A greater absorbance is observed when $TiO_2$ is modified by $SiO_2$/QD@$SiO_2$ NPs. Both types of films, with and without N719 dye, exhibit better UV-vis absorbance than the corresponding films without a layer of $SiO_2$/QD@$SiO_2$ NPs. To confirm the effect of $SiO_2$ core, photoanode modified with $SiO_2$ core only was prepared by similar procedure. There is no significant increase in absorption spectra of $SiO_2$-modified photoanode.

The UV-vis diffused reflectance spectra were measured to find out the effect of light scattering by relatively large particles (~150 nm). However, as shown in Figure 2.5 there was no significant difference among the samples. Smaller size (~120 nm) than incident light wavelength (300~800 nm) could not affect the light path way.

35
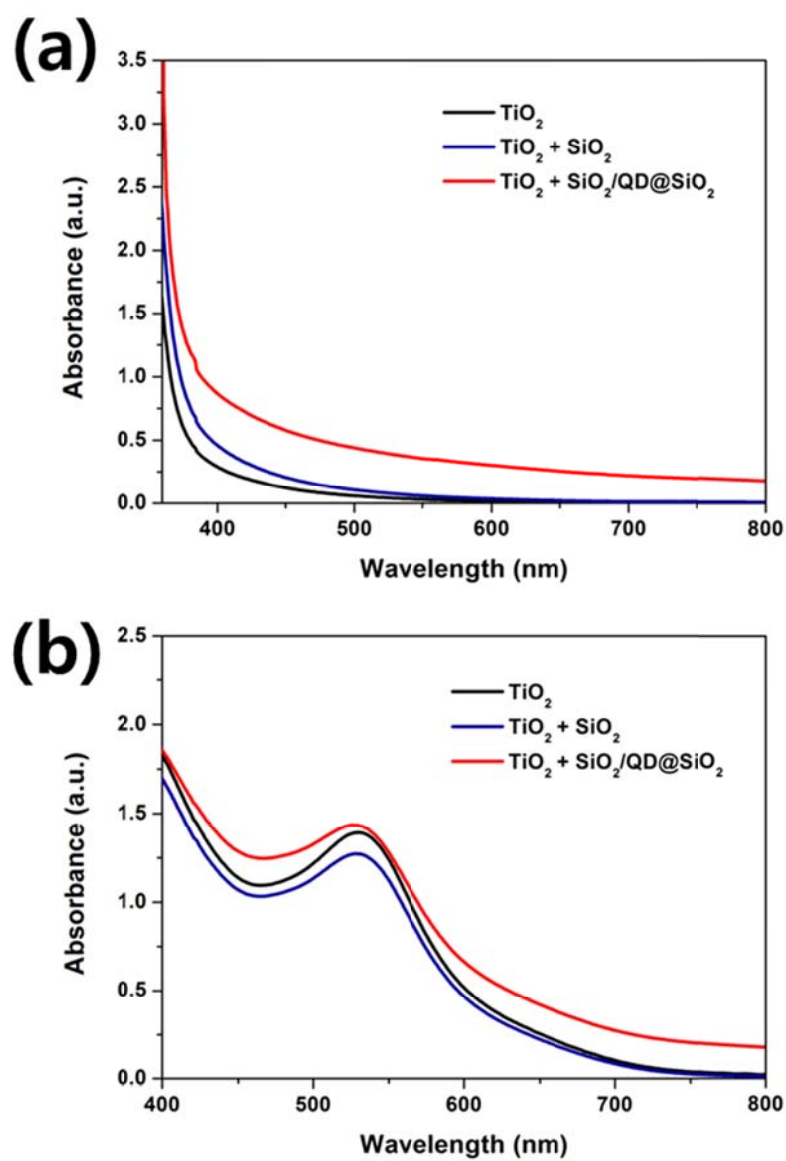
**Figure 2.4 UV-vis absorption spectra of (a) photoanodes without N719 dye, (b) photoanodes with N719 dye.**
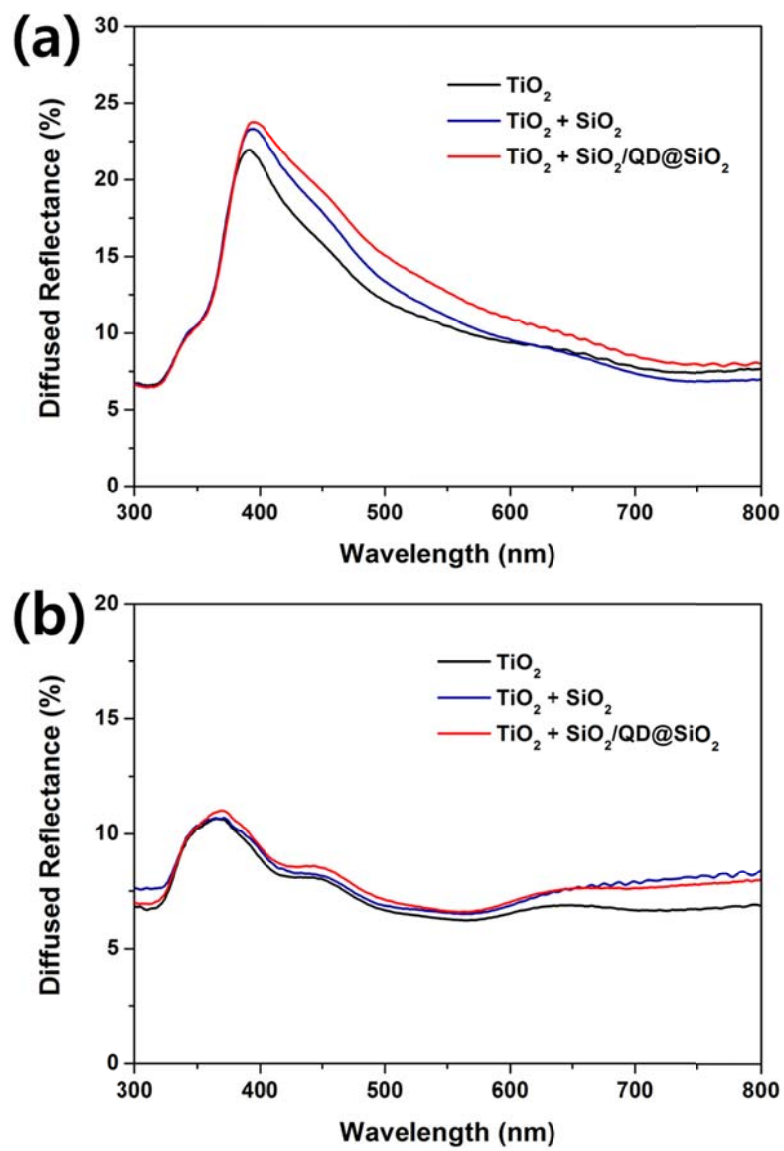
**Figure 2.5 UV-vis diffused reflectance spectra of (a) photoanodes without N719 dye, (b) photoanodes with N719 dye.**

### 2.3.3 Confocal laser scanning microscopy (CLSM)

We further analyzed the photoanodes using confocal laser scanning microscopy (CLSM) to find out photoluminescence of $SiO_2$/QD@$SiO_2$ NPs in the cell. We obtained confocal microscopy image with 405 nm laser and fixed master gain of illumination power of 478 for detailed comparison with fluorescence intensity. The fluorescence images were recorded at 570~660 nm. The incident laser illuminated samples from front side of FTO glass (front illumination, Figure 2.7) and from the opposite direction which passes $SiO_2$/QD@$SiO_2$ layer (back illumination Figure 2.8).

No fluorescence was detected in all samples without $SiO_2$/QD@$SiO_2$ NPs. In photoanodes that contain $SiO_2$/QD@$SiO_2$ NPs, the fluorescence with narrow emission peak of 620 nm was confirmed by Lambda scan mode. (Figure 2.6) The fact that the QDs in the working electrode display fluorescence indicates that they are in a stable state. Additionally, the results of front illumination indicate that the light radiation could reach the $SiO_2$/QD@$SiO_2$ NPs. As shown in Figure 2.7 and 2.8., the fluorescence from $SiO_2$/QD@$SiO_2$ NPs was evenly spread across the photoanodes. The higher fluorescence mean intensity was observed when the laser illuminated through $SiO_2$/QD@$SiO_2$-side (back illumination), this result came from absorption disturbance of FTO glass and

38

TiO$_2$ thin film.

Moreover, there was a marked reduction in mean fluorescence intensity after dye-adsorption. It is evidence of energy transfer. Generally, energy transfer related to fluorescence is divided into two mechanisms: radiative energy transfer and non-radiative energy transfer (Förster resonance energy transfer). According to the theory of Förster resonance energy transfer (FRET), when the absorption spectrum of the energy acceptor overlaps significantly the fluorescence emission spectrum of the energy donor and when the donor and acceptor are close enough, the emission of the energy donor will be quenched by the acceptor.[56] In our system, the absorption spectrum of N719 overlaps the fluorescence emission spectrum of SiO$_2$/QD@SiO$_2$. However, it is estimated that energy from QDs was not transferred to N719 through FRET, but through radiative energy transfer. The FRET efficiency ($E$) is expressed by the following equation.

$$E = \frac{1}{1 + (r/R_0)^6}$$

Where $r$ is the donor-to-acceptor separation distance, $R_0$ is the Förster distance of pair, the distance at which the energy transfer efficiency is 50%.

As shown in the equation, $E$ is in inverse proportion to the $r^6$. It is well-known that FRET is dominant when the donor and the acceptor are close within 10 nm. In this system, QDs (donor) and N719 dye (acceptor) were separated by the $SiO_2$ shell and electrolyte. It means that most fluorescence re-emitted by $SiO_2$/QD@$SiO_2$ was absorbed by N719 dye by radiative energy transfer.

The silica particle with 520 nm emission-quantum dots was also fabricated to match with the absorption of N719 dye.(Figure 1.5) However, in the photoanode, it exhibited very weak photoluminescence in back and front illumination because of its low internal quantum yield.(Figure 2.9)
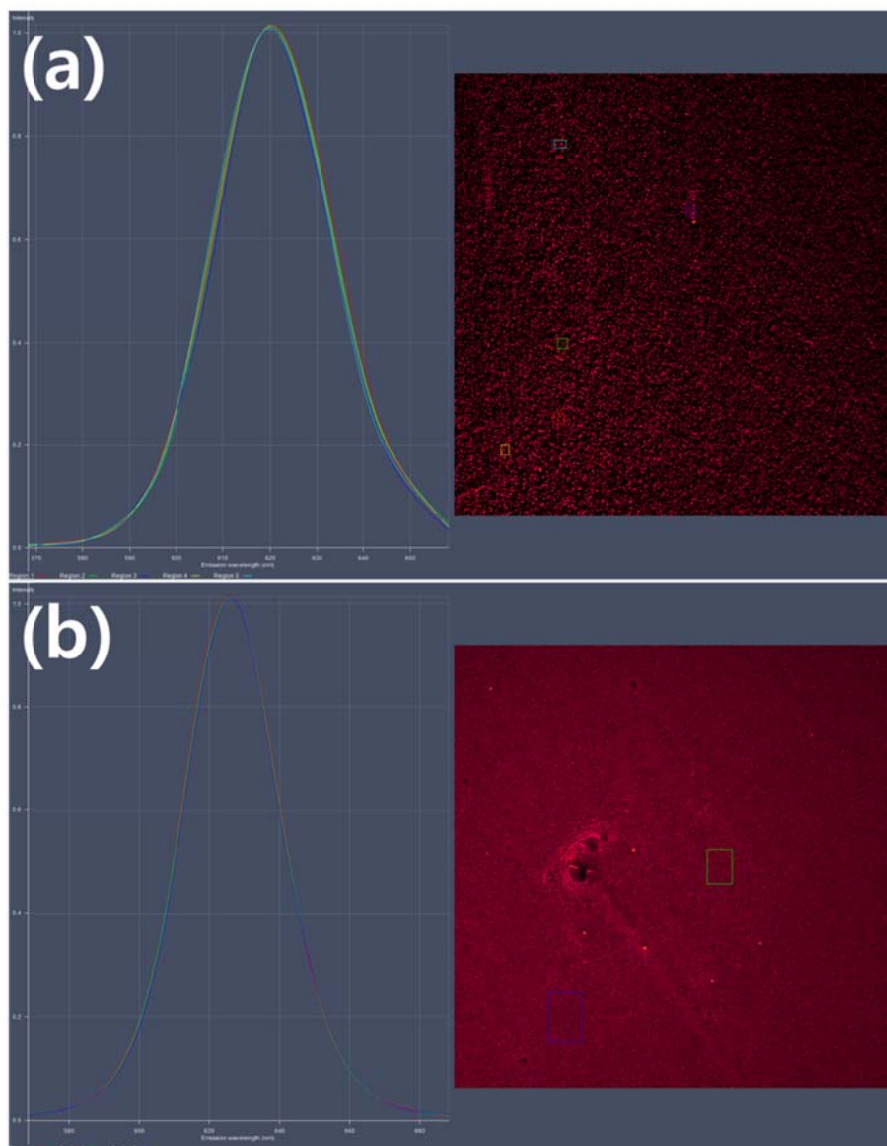
**Figure 2.6 Lambda scan profiles of (a) photoanode without N719 dye, (b) photoanode with N719 dye.**
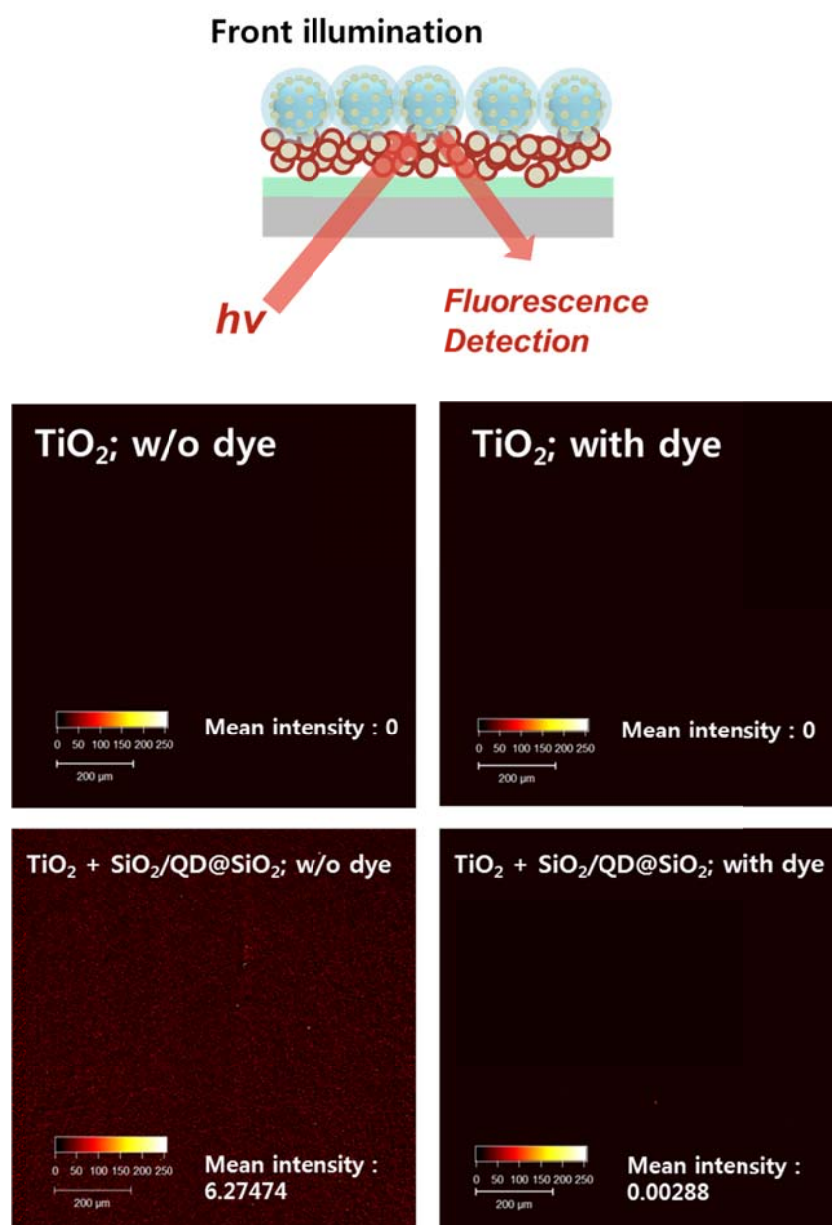
**Figure 2.7 Confocal laser scanning microscopy images (Front illumination)**
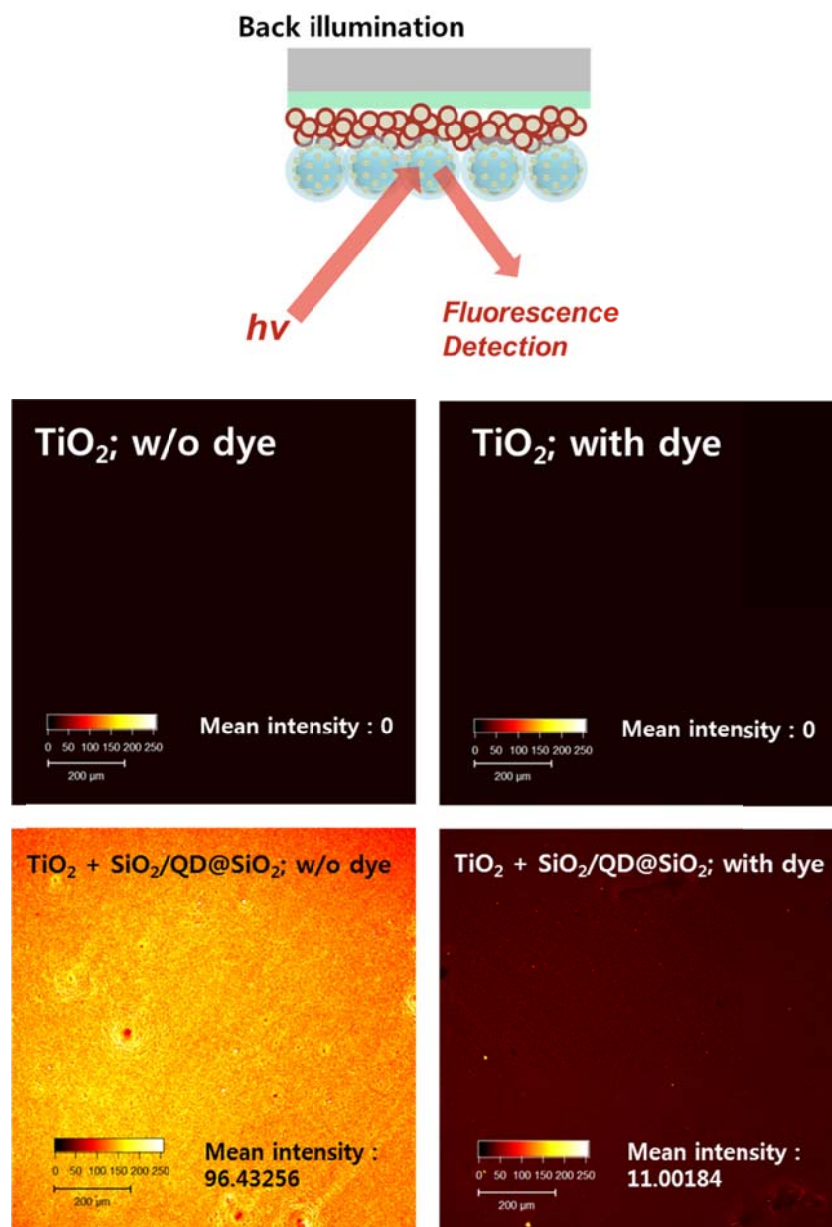
**Figure 2.8 Confocal laser scanning microscopy images (Back illumination).**
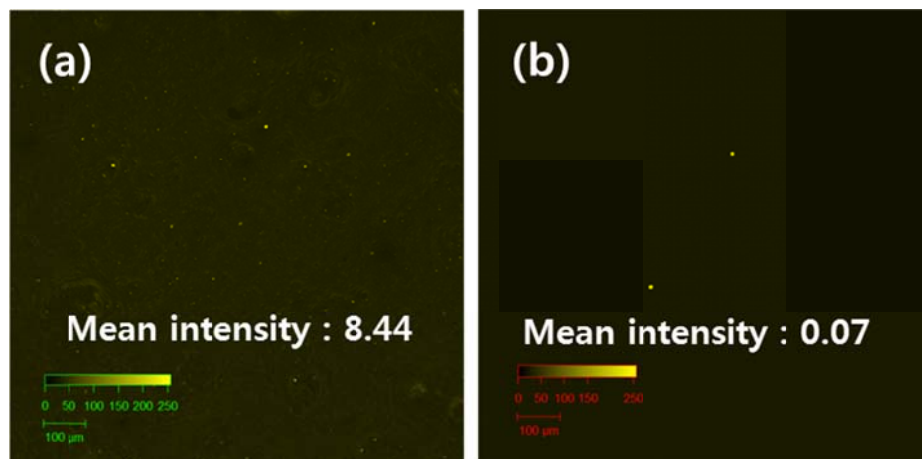
**Figure 2.9 Confocal laser microscopy image of thin-film with SiO$_2$/QD@SiO$_2$ (520 nm) (a) back illumination, (b) front illumination.**

### 2.3.4 Photovoltaic characteristics

Figure 2.9 shows the current density-voltage ($J-V$) curves of DSSCs; their properties are summarized in Table 2.1. To demonstrate the increasing efficiency of the $SiO_2$/QD@$SiO_2$ DSSCs, an unmodified DSSC and $SiO_2$-modified DSSC were also fabricated for comparison. The unmodified DSSC exhibited a short-circuit current density ($J_{SC}$) value of 9.60 mA/cm$^2$ and a power conversion efficiency of 5.38%. In comparison, the $SiO_2$/QD@$SiO_2$ DSSC showed an increased efficiency value of 5.86% because of the increased $J_{SC}$ (10.62 mA/cm$^2$). $SiO_2$-modified DSSC exhibited practically same performance with unmodified DSSC. Therefore, it was concluded that $SiO_2$ core did not contribute to enhanced efficiency. The fabricated solar cells were analyzed using incident photon-to-current efficiency (IPCE) spectroscopy (Figure. 2.10). The IPCE spectrum of the $SiO_2$/QD@$SiO_2$ DSSC was better than that of the unmodified DSSC and $SiO_2$-modified DSSC across a broad wavelength range, indicating the positive effect of the light harvesting layer.

The extinction coefficient of N719 at wavelength of 620 nm that is re-emitted by QDs is not high enough to attain significant enhancement of light utilization. To investigate the effect of re-emitted light by $SiO_2$/QD@$SiO_2$,

DSSC using unsymmetrical squaraine dye 5-carboxy-2-[[3-[(2,3-dihydro-1, 1-dimethyl-3-ethyl-1H-benzo[e]indol-2-ylidene)methyl]-2-hydroxy-4-oxo-2-cyclobuten-1-ylidene]methyl]-3,3-dimethyl-1-octyl-3H-indolium (SQ2) was fabricated. SQ2 dye is an organic sensitizer that mainly absorbs far-red light (wavelength of 550~710 nm) and possesses a higher extinction coefficient at 662 nm.[57] From its optical properties, the absorption range of SQ2 dye is well matched with emission wavelength of $SiO_2/QD@SiO_2$. The chemical structures of SQ2 dye and absorption spectra are shown in Figure 2.11.

  The photoanode composed of nanocrystalline $TiO_2$ and $SiO_2/QD@SiO_2$ were prepared using a previously mentioned procedure. The electrodes were immersed into the SQ2 dye solution composed of 0.1 mM with 10 mM of 3α, 7α -dihydroxy-5 $\beta$ -cholanic acid (chenodeoxycholic acid, CDCA) in ethanol and kept at room temperature for 4 h. CDCA was used as co-adsorbent in dye solution to prevent aggregation of dye molucules. Table 2.2 and Figure 2.12 shows the photovoltaic performance of SQ2 sensitized solar cells with or without $SiO_2/QD@SiO_2$. For $TiO_2$ film without $SiO_2/QD@SiO_2$, the short-circuit current density ($J_{SC}$) of 2.61 mA/cm$^2$ was obtained, whereas $TiO_2$ film with $SiO_2/QD@SiO_2$ showed 3.86 mA/cm$^2$. By using $SiO_2/QD@SiO_2$, significant improvement (48%) in $J_{SC}$ was observed, and this led to a 55% increase in the power conversion efficiency of the cell as a consequence. This

46

result is solid evidence that QDs acted as extra light re-emitter in the cell. Figure 2.13 shows the long-term stability of the $SiO_2/QD@SiO_2$ DSSC in an iodide/triiodide-based electrolyte. The performance of $SiO_2/QD@SiO_2$ DSSC was measured under air mass 1.5 and stored under dark (soaking) conditions. Variations in the efficiency and $J_{SC}$ were investigated as a function of time. Even after 168 h, the efficiency and $J_{SC}$ showed similar values, indicating that quantum dots coated with a silica shell remain stable in the iodide/triiodide-based electrolyte. Thus, it can be concluded that the $SiO_2/QD@SiO_2$ NPs in a DSSC can act as a light-harvesting layer, because they increase the efficiency and are stable for a long duration.

**Table 2.1 Photovoltaic parameters of dye-sensitized solar cells.**

| Photoanode | $J_{SC}$ (mA/cm$^2$) | $V_{OC}$ (V) | ff | $\eta$ (%) |
|---|---|---|---|---|
| TiO$_2$ | $9.60 \pm 0.44$ | $0.74 \pm 0.01$ | $0.76 \pm 0.02$ | $5.38 \pm 0.20$ |
| TiO$_2$ + SiO$_2$ | $9.84 \pm 0.55$ | $0.73 \pm 0.01$ | $0.74 \pm 0.03$ | $5.33 \pm 0.40$ |
| TiO$_2$ + SiO$_2$/QD@SiO$_2$ | $10.62 \pm 0.52$ | $0.74 \pm 0.01$ | $0.75 \pm 0.02$ | $5.86 \pm 0.03$ |
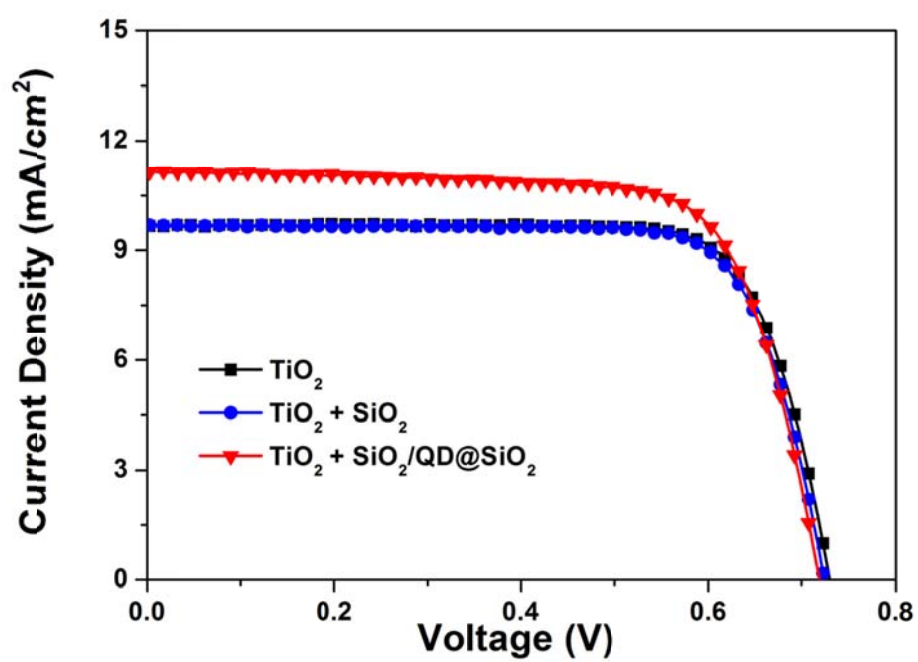
**Figure 2.10 *J-V* curves of dye-sensitized solar cells.**
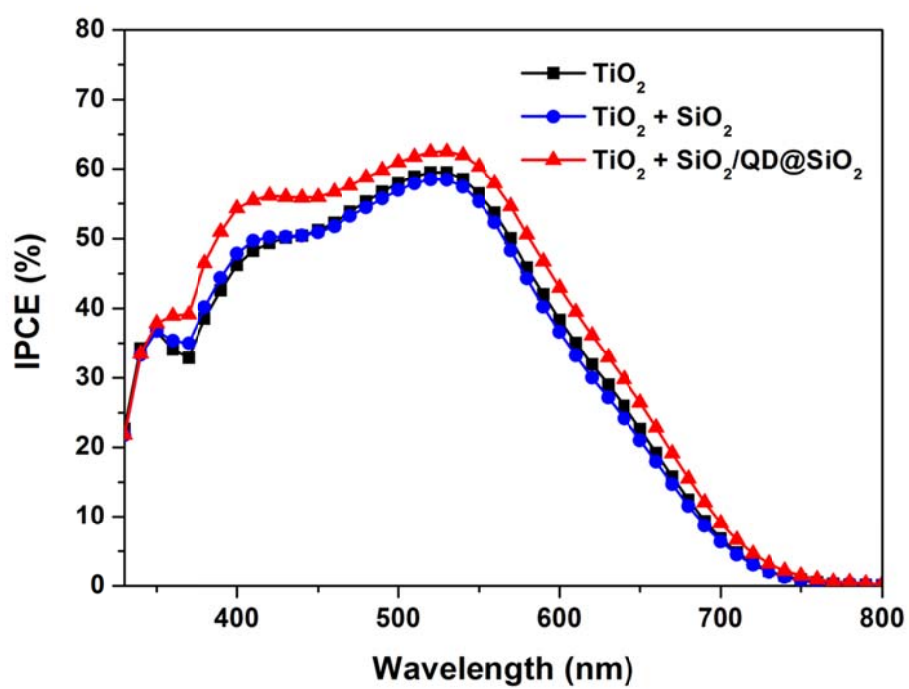
**Figure 2.11 Incident photon-tocurrent conversion efficiency (IPCE) spectra of DSSCs.**
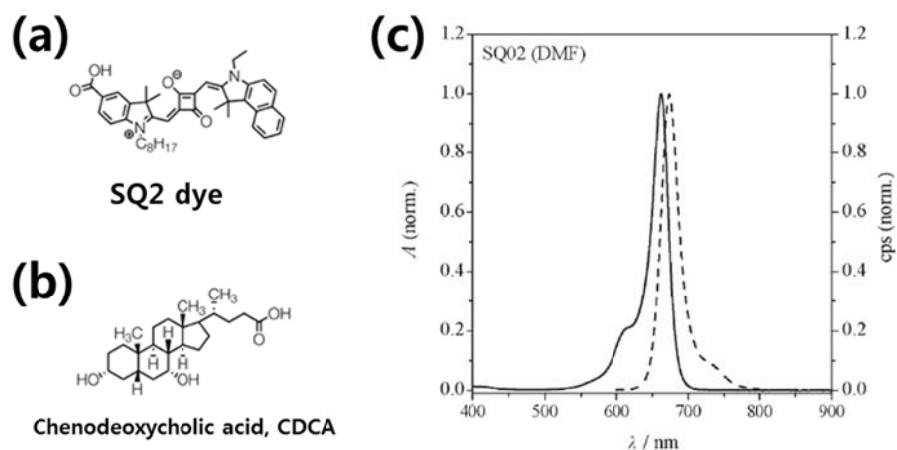
**Figure 2.12 Chemical structure of (a) SQ2 dye, (b) chenodeoxycholic acid, and (c) normalized UV-vis absorption (solid line)/emission (dash line) spectra of SQ2 in DMF. (ref. 47)**

**Table 2.2 Photovoltaic parameters of dye-sensitized solar cells using SQ2 dye.**

| Photoanode | $J_{SC}$ (mA/cm$^2$) | $V_{OC}$ (V) | ff | $\eta$ (%) |
|---|---|---|---|---|
| **TiO$_2$ (SQ2)** | 2.61 ± 0.32 | 0.60 ± 0.01 | 0.73 ± 0.01 | 1.13 ± 0.15 |
| **TiO$_2$ + SiO$_2$ (SQ2)** | 2.89 ± 0.23 | 0.60 ± 0.02 | 0.71 ± 0.04 | 1.24 ± 0.20 |
| **TiO$_2$ + SiO$_2$/QD@SiO$_2$ (SQ2)** | 3.86 ± 0.19 | 0.62 ± 0.01 | 0.73 ± 0.02 | 1.75 ± 0.15 |
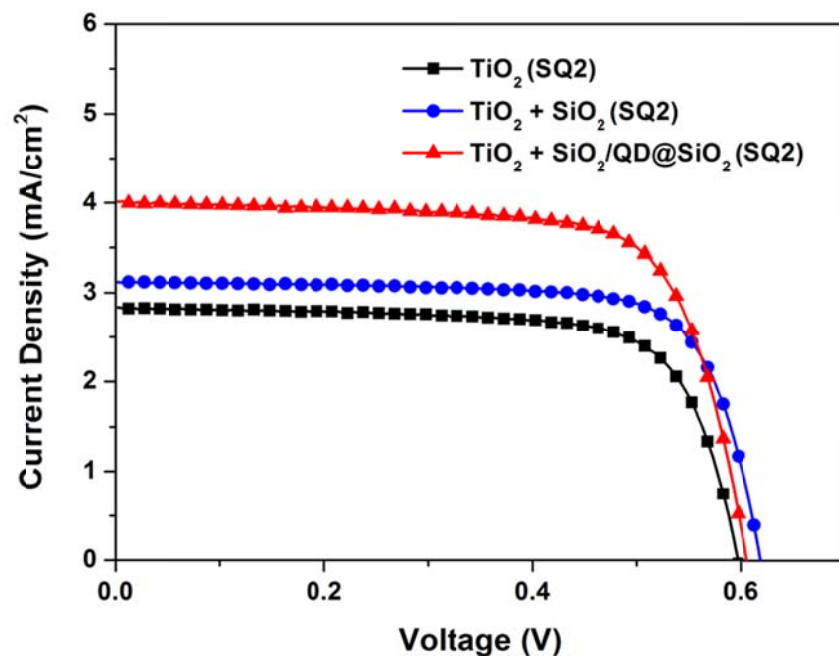
**Figure 2.13** *J-V cureves* **of DSSCs with SQ2 dye.**
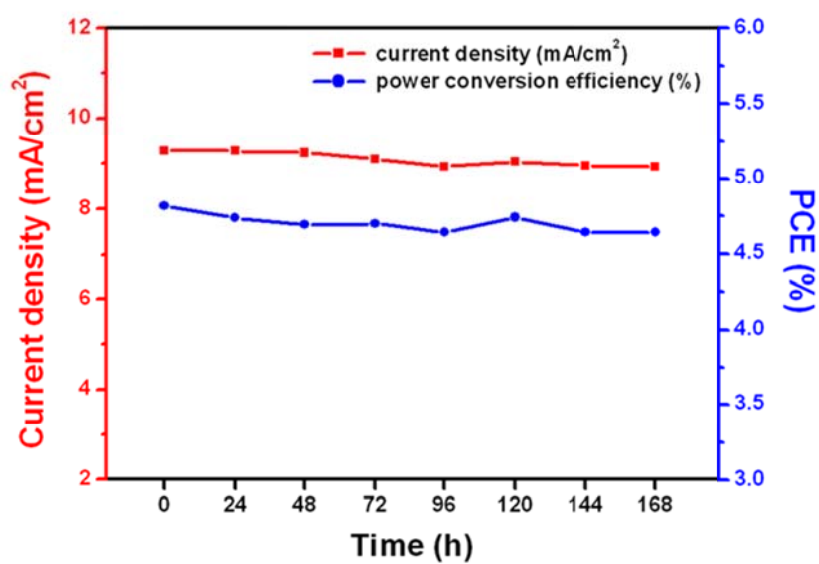
**Figure 2.14 Long-term stability of SiO$_2$/QD@SiO$_2$ DSSC.**

### 2.3.5 Photovoltaic performance without sensitizer

Different types of solar cells—without dye and with $SiO_2$/QD@$SiO_2$ NPs (1, 5, 10 and 15 times spin-coated) on the working electrode—were prepared for investigation of the role of $SiO_2$/QD@$SiO_2$ NPs (Table 2.3). The solar cell without $SiO_2$/QD@$SiO_2$ NPs exhibited the $J_{SC}$, $V_{OC}$, fill factor (*ff*), and efficiency ( $\eta$ ) values of 0.28 mA/cm$^2$, 0.57 V, 0.59, and 0.10% respectively. For the same set of parameters, the DSSC with $SiO_2$/QD@$SiO_2$ NPs (15 times) showed the corresponding values of 0.35 mA/cm$^2$, 0.60 V, 0.58, and 0.12%, respectively.

The UV-vis absorption of the photoanode film was increased with an amount of $SiO_2$/QD@$SiO_2$ NPs (Figure 2.14). However the photovoltaic parameters were not significantly changed by $SiO_2$/QD@$SiO_2$ NPs without dye, suggesting that $SiO_2$/QD@$SiO_2$ NPs did not affect the solar cell as sensitizers. Though $SiO_2$/QD@$SiO_2$ NPs could absorb the incident light and re-emit by fluorescence, it did not generate photoelectrons. Thus, we verified that the main role of $SiO_2$/QD@$SiO_2$ NPs is not acting as co-sensitizers but as the harvesting layers of extra light.
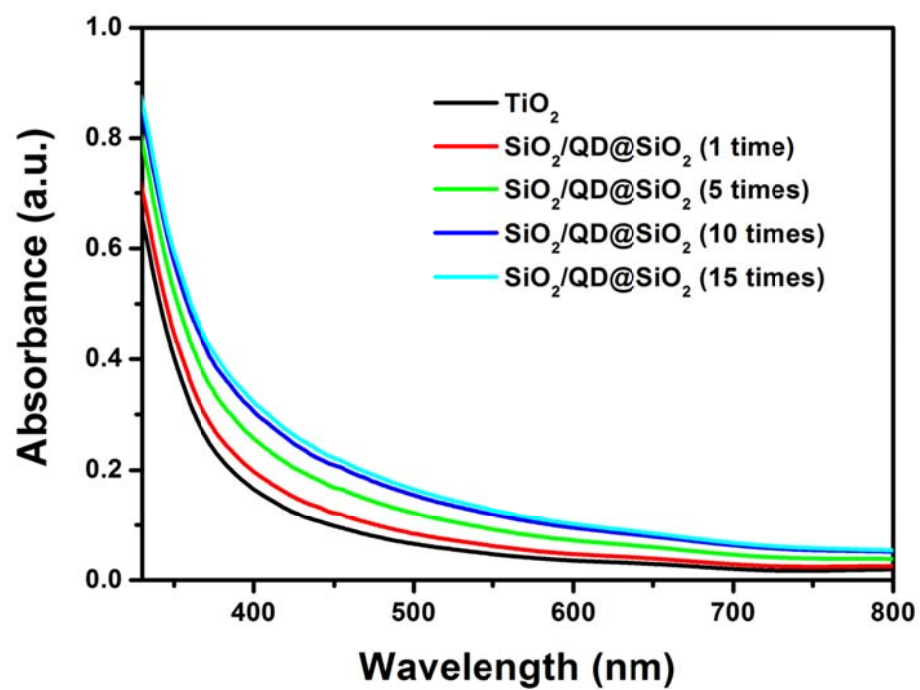
**Figure 2.15 UV-vis absorption spectra of photoanodes with increasing number of spin coating.**

**Table 2.3 Photovoltaic parameters of dye-sensitized solar cells without dye.**

| Photoanode | $J_{SC}$ (mA/cm$^2$) | $V_{OC}$ (V) | $ff$ | $\eta$ (%) |
|:---:|:---:|:---:|:---:|:---:|
| TiO$_2$ | 0.28 | 0.57 | 0.59 | 0.10 |
| TiO$_2$ + SiO$_2$/QD@SiO$_2$ (1 time) | 0.30 | 0.59 | 0.58 | 0.10 |
| TiO$_2$ + SiO$_2$/QD@SiO$_2$ (5 times) | 0.43 | 0.63 | 0.62 | 0.17 |
| TiO$_2$ + SiO$_2$/QD@SiO$_2$ (10 times) | 0.35 | 0.61 | 0.59 | 0.13 |
| TiO$_2$ + SiO$_2$/QD@SiO$_2$ (15 times) | 0.35 | 0.60 | 0.58 | 0.12 |

## 2.4 Conclusions

In conclusion, we fabricated silica-coated quantum dot-embedded silica nanoparticles ($SiO_2$/QD@$SiO_2$ NPs) and incorporated them into a dye-sensitized solar cell system for enhancing the light utilization in the photoanode. The prepared $SiO_2$/QD@$SiO_2$ NPs showed high extinction properties and excellent chemical stability without siginicant loss of quantum yields. UV-vis light absorption in the photoanode thin-film was improved by introducing $SiO_2$/QD@$SiO_2$ NPs as light reservoir. Confocal laser scanning microscopy image of $SiO_2$/QD@$SiO_2$-modified electrode indicated that the light radiation could reach the $SiO_2$/QD@$SiO_2$ NPs and the fluorescence from QDs was absorbed by nearby dyes. A DSSC with $SiO_2$/QD@$SiO_2$ NPs exhibited better efficiency than the corresponding unmodified DSSC. Moreover, as the silica shell protected the QDs from degradation in an iodide/triiodide-based electrolyte, the values of $J_{SC}$ and $\eta$ in the $SiO_2$/QD@$SiO_2$ DSSC were retained for (at least) 168 h. Moreover, $SiO_2$/QD@$SiO_2$ NPs did not work as sensitizers but as the harvesting layers of extra light. We expect that our methods can be applied to other types of solar cells to increase their efficiency. The synergistic effect of matching the wavelength of light emitted by QDs and the absorbance wavelength of dyes on the enhancement of DSSC efficiency is expected.

# Chapter 3. Plasmon-enhanced dye-sensitized solar cells

## 3.1 Introduction

When free electrons in metal nanoparticles are excited by incident light, collective electron charge oscillation called localized surface plasmon resonance (LSPR) occurs.[58] This phenomenon enhances the near-field amplitude and generates the plasmonic scattering at the resonance wavelength, which has been applied on surface plasmon resonance biosensors[59,60], surface-enhanced Raman scattering spectroscopy (SERS) based analysis,[61,62] nanoscale optical devices,[63] and photocatalysts.[64-67] Many researchers have attempted to utilize LSPR for various types of photovoltaic devices including DSSCs in order to improve light absorption by these devices.[68]

Conventionally, surface plasmon resonance can offer three ways of enhancing photovoltaic performance. First, metallic nanoparticles can be used as sub-wavelength antennas in which the plasmonic near-field is coupled to the sensitizer, increasing its effective absorption cross-section. (Figure 3.1(a)) Second, metallic nanoparticles can be used as subwavelength scattering

elements to trap propagating waves from the incident light into sensitizer.(Figure 3.1(b)) Third, a metallic film on the back surface of photovoltaic semiconductor layer can couple incident light into surface plasmon polaritons modes supported at the interface . (Figure 3.1 (c))

  In previous studies on utilizing LSPR for DSSCs, individual $TiO_2$ (or $SiO_2$)-coated noble metal NPs were incorporated into $TiO_2$ photoanodes, and the cell performance was enhanced via plasmon-enhanced absorption by sensitizers.[69-73] However, performance enhancement due to individual gold or silver NPs is commonly restricted to a particular wavelength region. Generally, the plasmonic absorption characteristics of metal NPs can be easily modulated by controlling their size and shape.[74] In addition, the use of an assembly of metal NPs gives rise to plasmon coupling, which contributes to stronger and broader plasmonic absorption.[75,76] Recently, Sheehan *et al*. reported a coupled plasmonic system for DSSCs that can lead to broadband plasmonic enhancement when used with aggregates composed of core-shell-shell $Au@SiO_2@TiO_2$ nanostructures.[77] However, the method using aggregates could not control the size or shape of particles precisely. Therefore, strategies for incorporating plasmonic nanostructures, which are capable of maximizing the enhancement in broad light absorption, are crucial for practical photovoltaic devices.

Herein, we demonstrate a new approach for obtaining plasmon-enhanced DSSCs by utilizing $SiO_2$ spheres decorated with tightly assembled silver NPs ($SiO_2$-t-Ag@$SiO_2$). $SiO_2$ shell was chosen in order to distinguish plasmonic effect and electron charging effect. It was reported that electron charging effect is dominant when $TiO_2$ shell is coated on metal nanoparticles. A schematic illustration of the photoanode employed in this study is shown in Figure 3.2 Local electric field (E-field) enhancement and plasmonic scattering from tightly assembled silver NPs improved the cell performance by increasing the light utilization throughout the wide visible light range. Consequently, the overall power conversion efficiency of the cell increased upon the addition of $SiO_2$-t-Ag@$SiO_2$, and this was mainly due to the improvement in the photocurrent density owing to plasmonic effects of tightly assembled silver NPs.
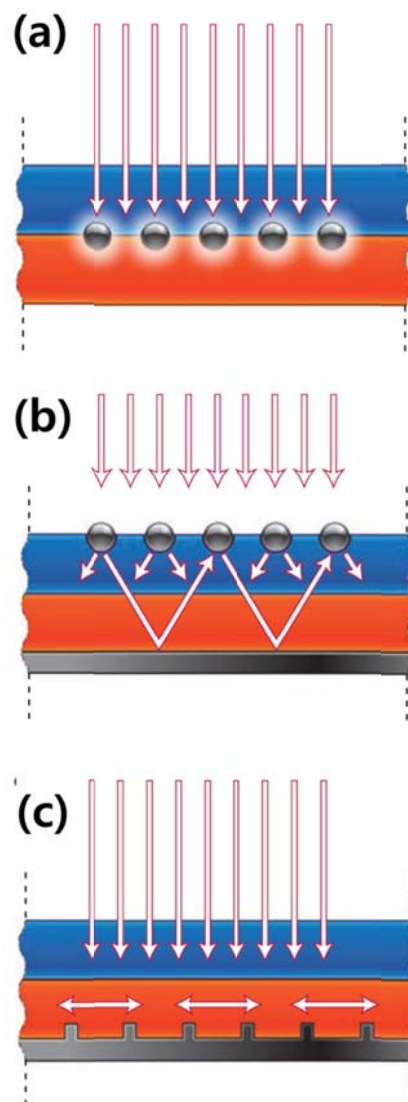
**Figure 3.1 Plasmonic light-trapping geometries for solar cells. (a) light trapping by the excitation of localized surface plamons , (b) light trapping by scattering from metal nanoparticles, (c) light trapping by the excitation of surface plasmon polaritons at metal/semiconductor interface. (ref. 68)**
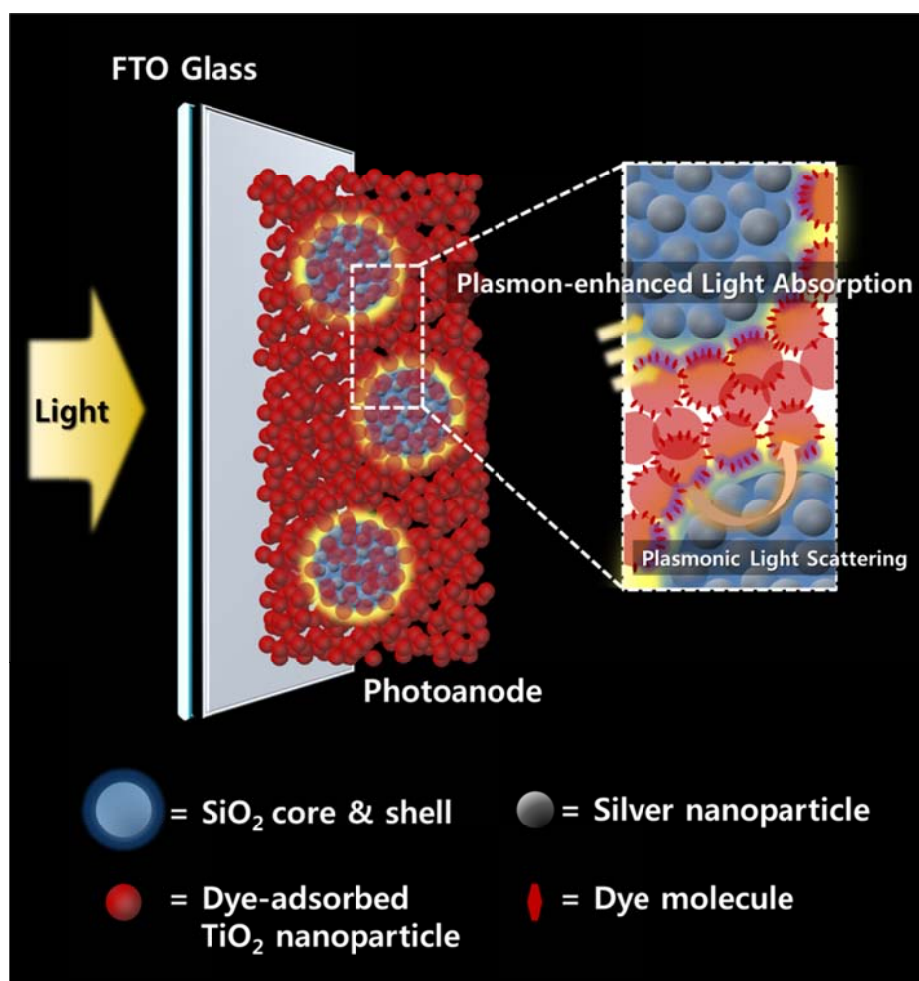
**Figure 3.2 Schematic illustration of a photoanode with SiO$_2$ spheres decorated with tightly assembled silver nanoparticles (SiO$_2$-t-Ag@SiO$_2$).**

## 3.2 Experimental section

### 3.2.1 Materials

Tetraethylorthosilicate (TEOS), 3-mercaptopropyl trimethoxysilane (MPTS), ethylene glycol (EG), poly(vinyl pyrrolidone) (PVP, MW ~40,000), silver nitrate (AgNO$_3$, 99.99+%), octylamine (OA), and all components of electrolyte were purchased from Sigma-Aldrich and used without further purification. Ammonium hydroxide (NH$_4$OH, 27%) and ethanol (98%) were purchased from Daejung Chemical. N719 (cis-diisothiocyanato-bis(2,2'-bipyridyl-4,4'-dicarboxylato) ruthenium(II) bis(tetrabutylammonium)) dye was purchased from Solaronix.

### 3.2.2 Preparation of SiO$_2$ spheres decorated with assembled silver nanoparticles

Tetraethylorthosilicate (TEOS, 1.6 mL) was dissolved in 40 mL of absolute ethanol, followed by addition of a 3 mL portion of aqueous ammonium hydroxide (27%).[56] The resulting mixture was vigorously stirred using magnetic bar for 20 h at 25 °C. The resulting silica spheres were centrifuged

and then washed with ethanol five times to remove the excess reagents. These silica spheres were then functionalized with thiol group. Silica spheres (150 mg) were dispersed in 3 mL ethanol containing 150 μL of MPTS and 30 μL of aqueous ammonium hydroxide (27 %). The mixture was stirred for 12 h at 25 °C. The resulting MPTS-treated silica spheres were centrifuged and washed with ethanol several times. In order to fabricate $SiO_2$ spheres decorated with tightly assembled silver nanoparticles ($SiO_2$-t-Ag), 25 mg portion of MPTS-treated silica spheres was thoroughly dispersed in 100 mL of $AgNO_3$ solution (3.5 mM in ethylene glycol). An 82.7 μL of octylamine (5 mM) was then rapidly added into the MPTS-treated silica spheres dispersion. The resulting mixture was stirred for 1 h at 25 °C. Afterwards, $SiO_2$ spheres decorated with tightly assembled silver nanoparticles were centrifuged and washed with ethanol five times for purification. In case of $SiO_2$ spheres decorated with sparsely assembled silver nanoparticles ($SiO_2$-s-Ag), 50 mg of MPTS-treated silica spheres was used in the same reaction condition except amount of $SiO_2$ sphere.

For silica coating to $SiO_2$ spheres decorated with tightly assembled silver nanoparticles, a 1 mL portion of MPTS solution (2 mM in ethanol) was added into 1 mg of silver nanoparticles-decorated silica spheres. The resulting dispersion was shaken for 1 h at 25 °C. The silver nanoparticles-decorated

65

silica spheres were transferred to 50 mL of 2-propanol with 1 mg of PVP (MW ~40,000). A 2 ml of ammonium hydroxide was added to the reaction mixture under vigorous stirring, followed by the addition of 250 μL of TEOS solution (TEOS/2-propanol, 0.8 v/v) in two separate portions with a time interval of 30 min. After adding the TEOS, the mixture was allowed to react for 12 h. Finally, the resulting silica coated $SiO_2$ spheres decorated with tightly assembled silver nanoparticles ($SiO_2$-t-Ag@$SiO_2$) were centrifuged and washed with ethanol five times.

### 3.2.3 Preparation of the photoanodes

F-doped $SnO_2$ (FTO) glass plates (8 $\Omega/cm^2$, Pilkington TEC glassTM) were cleaned in detergent solution using an ultrasonic bath for 20 min and washed with tap water and ethanol. The cleaned FTO glass plates were immersed in 40 mM $TiCl_4$ aqueous solution at 70 °C for 30 min and rinsed with DI water and ethanol. The photoanode pastes incorporating $SiO_2$-t-Ag@$SiO_2$ or $SiO_2$ were prepared by simple mixing process. The $SiO_2$-t-Ag@$SiO_2$ or $SiO_2$ in ethanol solutions ($SiO_2$ to $TiO_2$ ratio = 1, 3 and 5 wt%) were mixed with commercial $TiO_2$ pastes (Dyesol, DSL 18NR-T), and they were stirred for 2 h and dispersed several times by ultrasonicator (70% amplitude, on/off : 2/2 s, 3

66

min) . Then ethanol was removed by rotary evaporator. The photoanode films were prepared on TiCl$_4$-treated FTO plates by Doctor blade printing method, and annealed at 500 °C for 15 min. The thickness and the active area of photoanode films were controlled to 6 μm and 0.2025 cm$^2$, respectively.

### 3.2.4 Assembly of dye-sensitized solar cells

Pt counter electrodes were prepared by thermal deposition. A drop of 10 mM H$_2$PtCl$_6$ in 2-propanol was spread on FTO glass plate by spin coating followed by heating to 400 °C for 15 min. The prepared photoanode was assembled with counter electrode (with drilled hole) into sandwich-type cell using thermal adhesive film (Surlyn: 60 μm, Dupont). The electrolyte solution was prepared by mixing 0.60 M 1,2-dimethyl-3-propylimidazolium iodide, 0.05 M I$_2$, 0.10 M guanidinium thiocyanate and 4-tert-butylpyridine in a mixture of acetonitrile and valeronitrile (v/v, 85:15). Before the measurement of photovoltaic performance, a mask of 0.16 cm$^2$ was attached on the outside of FTO glass having the photoanode.

### 3.2.5 Instruments

UV-vis absorption spectra of the particles in solutions were collected by a UV-vis spectrometer (Mecasys Co. Ltd., Optizen 2120 UV). UV-vis absorption and reflectance spectra of the photoanodes were collected by UV-vis spectrometer (Jasco, V-670) with integrated sphere. A TEM images were obtained using EF-TEM (Carl Zeiss, LIBRA 120). The photovoltaic performance was measured using a 500 W xenon lamp (XIL model 05A50KS source measure units and an AM 1.5 filter) at a power of 100 mW/cm$^2$. The incident light intensity was adjusted with a silicon reference solar cell. The incident photon-to-current efficiency was measured using solar cell quantum efficiency measurement system (QEX7, PV measurements, Inc.).

## 3.3 Results and discussion

### 3.3.1 Preparation of SiO$_2$ spheres decorated with tightly assembled silver nanoparticles

Silica nanoparticles (SiO$_2$ NPs) were synthesized by the Stöber method,[46] and then thiol groups were introduced on the surface of SiO$_2$ NPs. The SiO$_2$ NPs had diameters of approximately 150–200 nm; the sizes of the SiO$_2$ NPs were large enough for sustaining a large number of silver nanoparticles (Ag NPs) at a time. Ag NPs with diameters of 20–30 nm were densely grown on the thiol-functionalized SiO$_2$ surfaces (SiO$_2$-t-Ag). Then they were coated with a SiO$_2$ shell (SiO$_2$-t-Ag@SiO$_2$) by a similar procedure for electronically and chemically insulating them. Figure 3.3(a) and 3.3(b) show transmission electron microscopy (TEM) images of SiO$_2$ spheres decorated with tightly assembled silver NPs before and after covering with a thin SiO$_2$ shell, respectively. Ag NPs on the SiO$_2$ core were covered with a ~5-nm-thick amorphous SiO$_2$ shell. To confirm the effect of coupled plasmon modes, individual silver nanoparticles and SiO$_2$ spheres decorated with sparsely assembled silver nanoparticles (SiO$_2$-s-Ag) were prepared by similar method.(Figure 3.4 (a) and 3.4(b) )
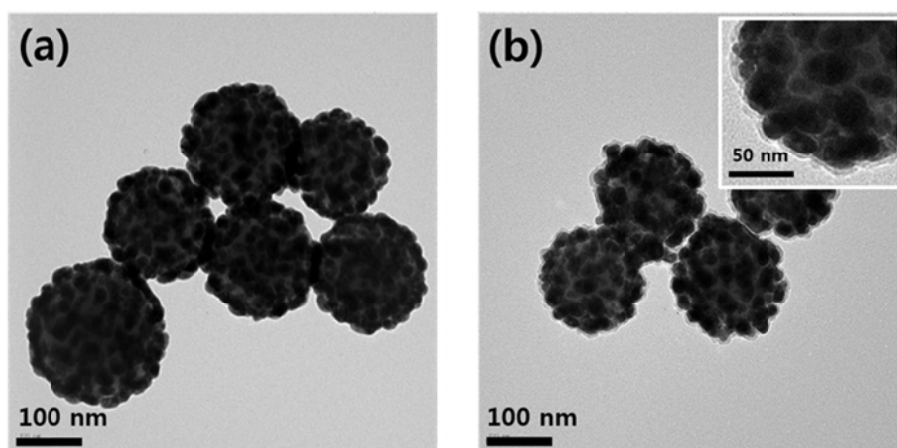
**Figure 3.3 TEM images of SiO$_2$ spheres decorated with tightly assembled silver nanoparticles (a) before and (b) after SiO$_2$ shell coating.**
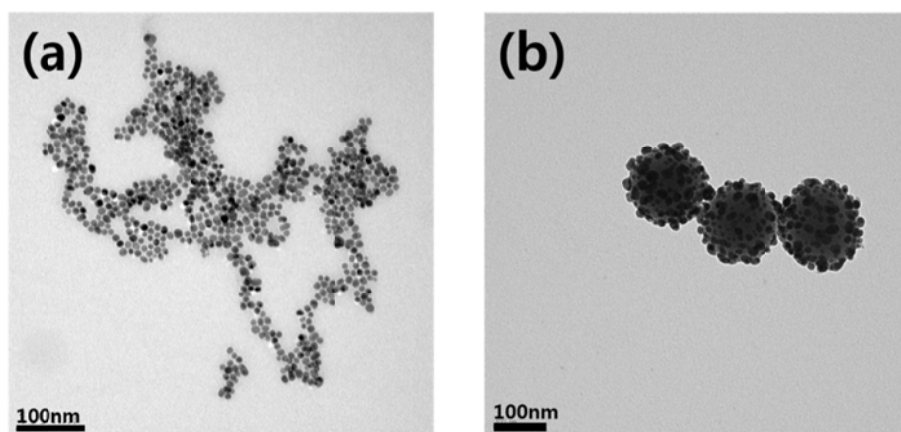
**Figure 3.4 TEM images of (a) individual Ag NPs and (b) SiO$_2$ spheres decorated with sparsely assembled silver nanoparticles (SiO$_2$-s-Ag).**

### 3.3.2 Discrete dipole approximation (DDA) simulation

The discrete dipole approximation (DDA) is a flexible and powerful technique for computing absorption and scattering of electromagnetic waves by targets of arbitrary geometry. The DDA simulation is one of the most popular methods in analyzing LSPR phenomenon. This method divides nanoparticles into a cubic array of dipoles, applied to calculating the total extinction efficiency (Q_tot), absorption efficiency (Q_abs), scattering efficiency (Q_sca), whether in one frequency or continuous spectrum. And this method is suitable for not only the single nanoparticle, but also the periodic array of nanoparticles.

In this work, DDA is used to simulate the LSPR of individual Ag NP, $SiO_2$ spheres decorated with sparsely assembled silver nanoparticles ($SiO_2$-s-Ag) and of $SiO_2$ spheres decorated with tightly assembled silver nanoparticles ($SiO_2$-t-Ag). We simulated the electric field distribution around the light-illuminated particles by using the DDSCAT 7.1 package. In simulation, isotropic dipoles are evenly placed in silver nanoparticles at dipole–dipole distances of 2 nm. Direction of incident light headed toward –z axis, and polarization of light was occurred in y axis. These silver nanoparticles were 20 nm in diameter, and the distance between silver nanoparticles is 2 and 10

72

nm in case of $SiO_2$-t-Ag and $SiO_2$-s-Ag respectively, and silica core was 160 nm in diameter. Overall amount of dipoles were 400,185 for $SiO_2$-t-Ag.(Figure 3.5(a)) From DDA simulation results, a stronger electric field than $SiO_2$-s-Ag was observed at the surface of $SiO_2$-t-Ag.(Figure 3.5(b) and 3.5(c)) Moreover, "Hot spots" which are regarded as the evidence of plasmon coupling were observed only in the result of $SiO_2$-t-Ag. In the results of individual Ag NP and $SiO_2$-s-Ag, the coupled plasmon mode that occurs when metal nanoparticles are adjacent to each other was not observed. For detailed analysis, electric field intensity distribution in $SiO_2$-t-Ag was simulated in terms of incident light wavelength. The overall field intensity was decreased with an increase of wavelength.(Figure 3.6) Also, the enhanced field was confirmed outside of the $SiO_2$ shell.(Figure 3.7(b) and 3.7(c))

Figure 3.8 shows calculated absorption and scattering efficiencies of $SiO_2$-t-Ag and $SiO_2$-s-Ag. At resonance wavelength, the plasmonic particles not only absorb but also scatter light efficiently. The localized surface plasmon of $SiO_2$-t-Ag is expected to offer increased dye absorption via the interaction of dye molecule dipole and the light trapping by plasmonic scattering. It can be seen the power of plasmonic light scattering decreased more rapidly than the power of absorption with increase of wavelength, and the ratio of integrated area between absorption and scattering of $SiO_2$-t-Ag is 6.3:3.7. As shown in

Figure 3.8(b), the overall power of electric field intensity of $SiO_2$-t-Ag is much higher than that of $SiO_2$-s-Ag.
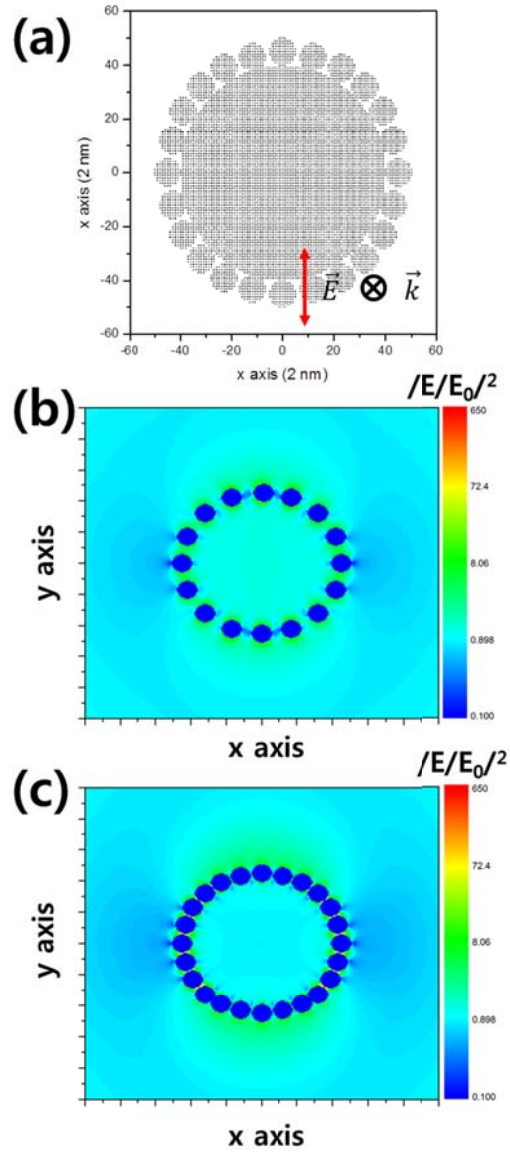
**Figure 3.5(a) Structure of simulated particle (SiO₂-t-Ag), electric field distribution of (b) SiO₂-s-Ag, (c) SiO₂-t-Ag.**
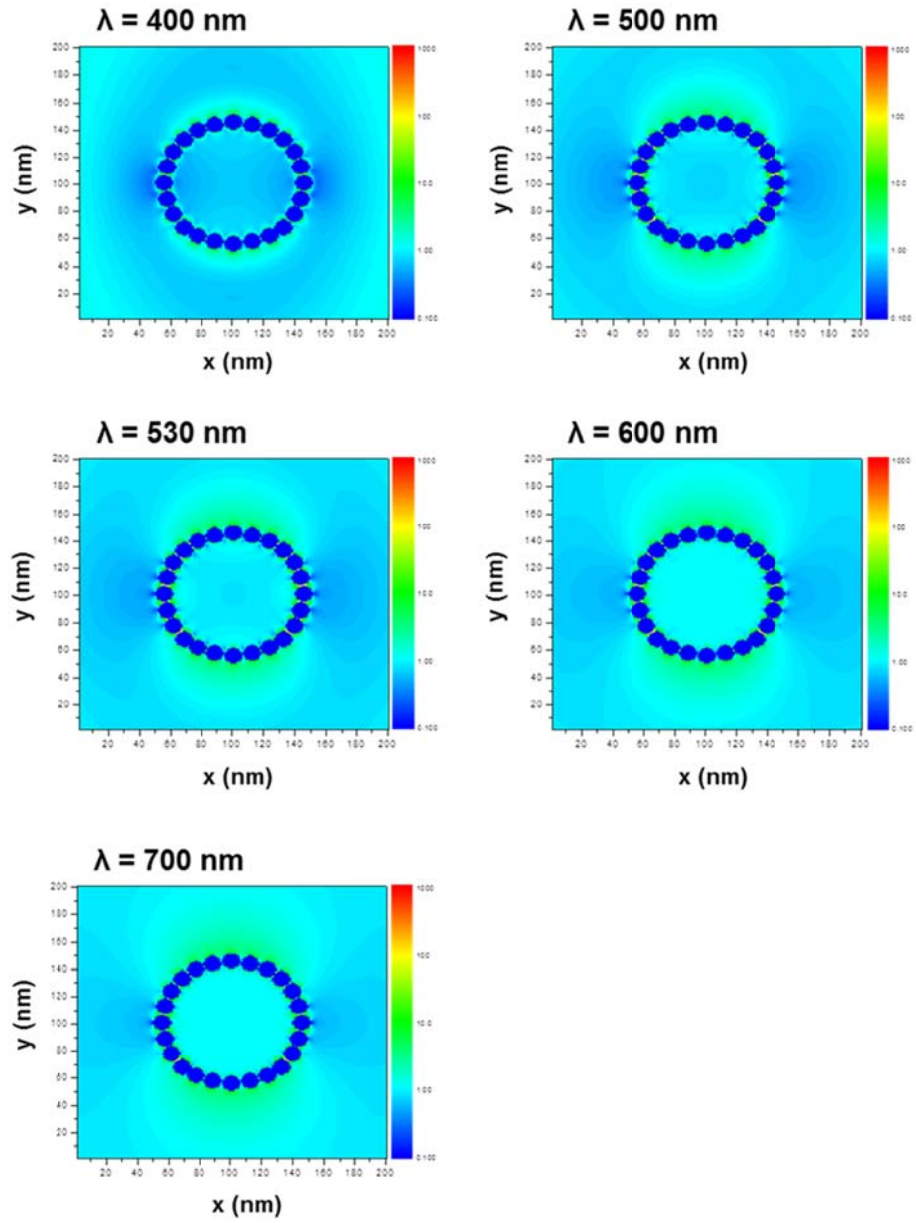
**Figure 3.6 Electric field intensity distribution in SiO₂-t-Ag.**
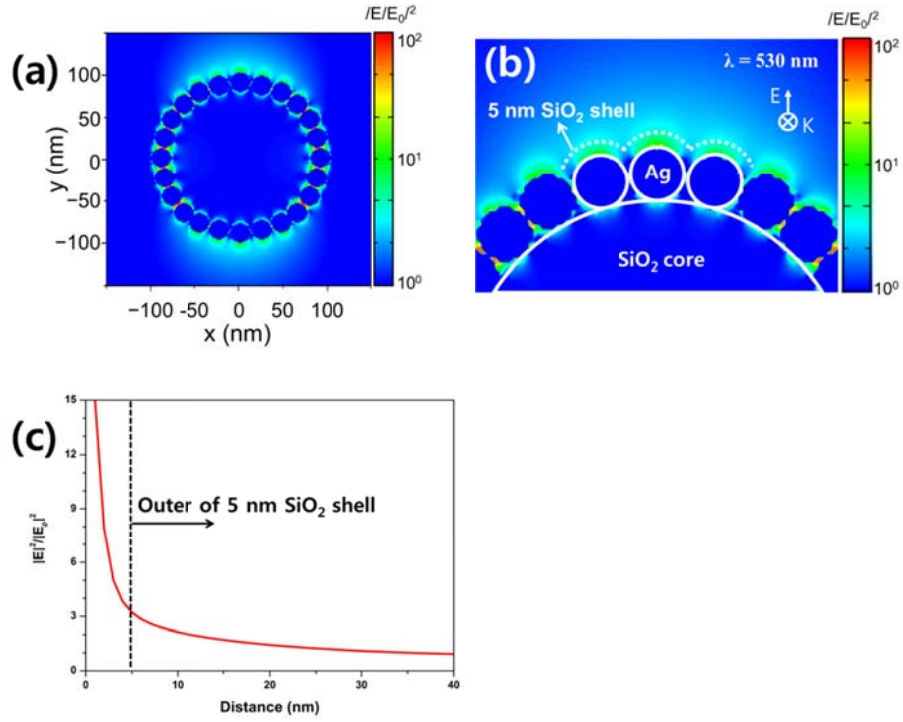
**Figure 3.7(a) Electric field intensity distribution in SiO₂ sphere decorated with silver nanoparticles, (b) showing a close up silver nanoparticle surface, (c) Intensity of electric fields with respect to the distance from silver nanoparticle.**
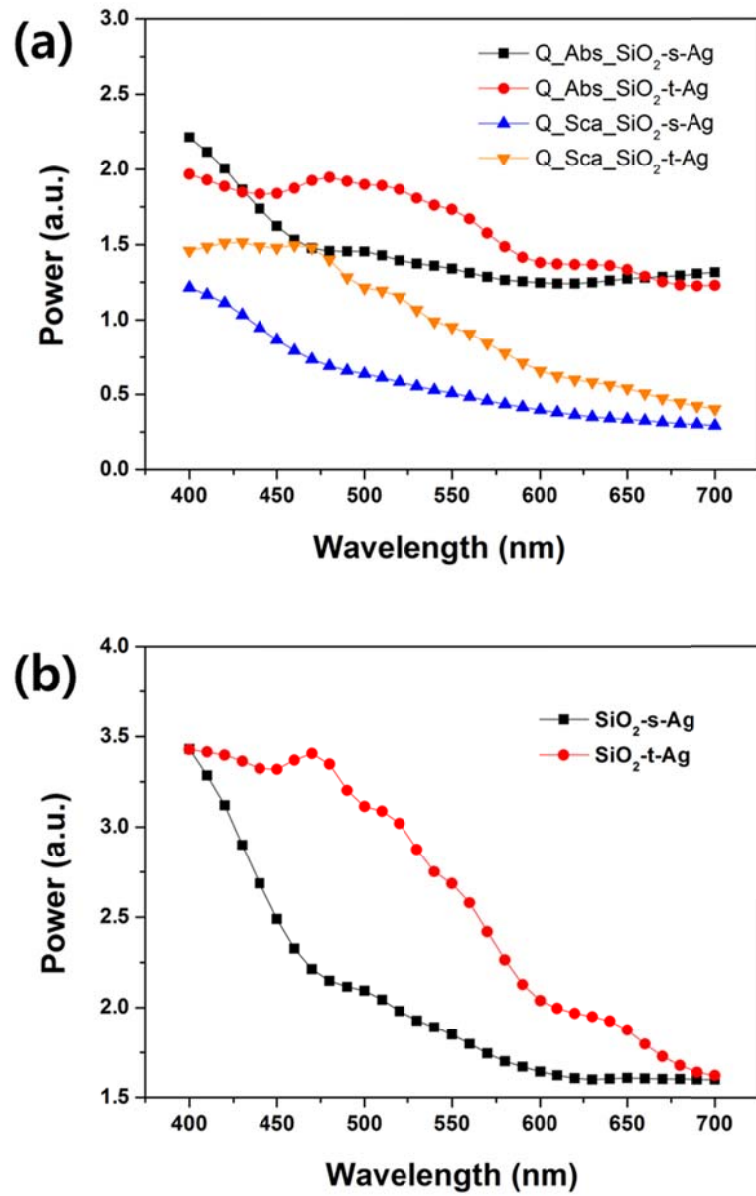
**Figure 3.8(a) Calculated absorption and scattering efficiency, (b) sum of Q_abs and Q_Sca.**

### 3.3.3 UV-vis absorption spectra of plasmonic particles in solution

Figure 3.9 shows UV-vis absorbance of the prepared NPs in ethanol before $SiO_2$ coating. Across the whole visible light region, $SiO_2$ spheres decorated with tightly assembled Ag NPs ($SiO_2$-t-Ag) exhibited novel plasmonic extinction that was different from that exhibited by individual Ag NPs and $SiO_2$-s-Ag that show a sharp peak at around 400 nm.

Generally, small nonaggregated spherical particles yield a single resonance peak. Therefore, this specific strong broadband absorption of $SiO_2$-t-Ag was due to plasmon coupling that originated from closely located Ag NPs. It was well known that the junction between adjacent nanoparticles, pairs, larger clusters, or even aggregate films of nanoparticles, can give rise to highly intense and localized electromagnetic fields when excited by incident light of the appropriate wavelength. The simplest description of this interaction, the coupling of two nearby oscillators, is in the coupling of two nearby dipoles. The interaction energy is given by $V \propto p_1 p_2/r^3$ where $p_1$ and $p_2$ are the magnitudes of the dipole moments and $r$ is the interparticle distance. This interaction energy is sufficiently strong in the case of nearly adjacent metallic nanoparticles to shift their resonant frequencies, resulting in new red-shifted and blue-shifted resonances relative to the resonance of each individual

79

nanoparticle. Generally, when gold or silver nanoparticles begin to aggregate, their optical spectrum acquires a new broadened peak, red-shifted significantly from the spectral peak of the absorption for the isolated nanoparticle.

In the UV-vis absorption spectra of $SiO_2$-t-Ag, red-shift from 410 nm to 580 nm was observed. It is obvious evidence of plasmon coupling between Ag NPs. Because a number of Ag NPs are closely located within 2 nm of interparticle distance, the electron oscillations of Ag NPs can be coupled on the $SiO_2$ core. In addition, on the basis of the absorption spectra of the NPs, it is expected that the LSPR of $SiO_2$-t-Ag can occur even in the near-infrared region. These UV-vis absorption results are in the good agreement with the DDA simulation.

At first, the effect of LSPR from $SiO_2$-t-Ag@$SiO_2$ on the absorption of N719 dye was investigated in solution. The LSPR effect in solution simulated the effect in plasmon-enhanced DSSCs, and the concentrations of $SiO_2$-t-Ag@$SiO_2$ and dyes were precisely controlled. As shown in Figure 3.10(a), the absorption of dye increased with the presence of $SiO_2$-t-Ag@$SiO_2$ in solution, and the absorption peak position slightly shifted from 530 nm to a shorter wavelength of 527 nm. Figure 3.10(b) represents net changes of dye absorption due to the presence of $SiO_2$-t-Ag@$SiO_2$. The optical enhancement

was decreased with amount of $SiO_2$-t-Ag@$SiO_2$, because of strong light absorption property of $SiO_2$-t-Ag@$SiO_2$. There is a close correspondence between relative changes of effective extinction coefficient of N719 dye and absorption spectra of dye. It also agrees with the previously reported observations on plasmon-enhanced dye absorption. The increase of absorption of dye molecules could be attributed to the interaction of dye molecule dipole and enhanced electric field surrounding $SiO_2$-t-Ag@$SiO_2$, together with the increase of plamonic light scattering also induced by LSPR.
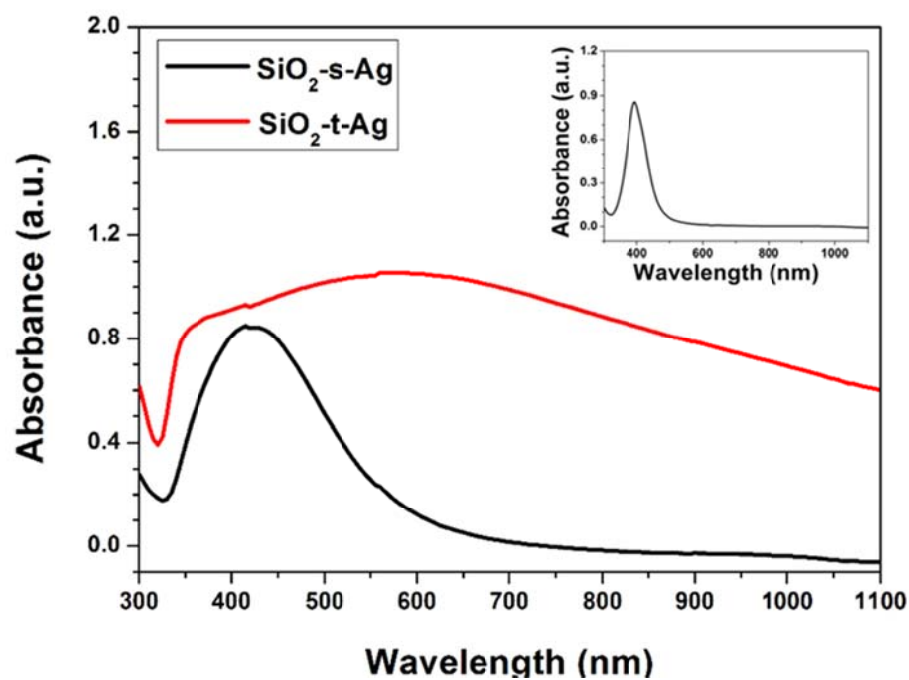
**Figure 3.9 UV-vis absorption spectra of SiO₂-t-Ag and SiO₂-s-Ag (inset: UV-vis absorption spectra of individual Ag NPs)**
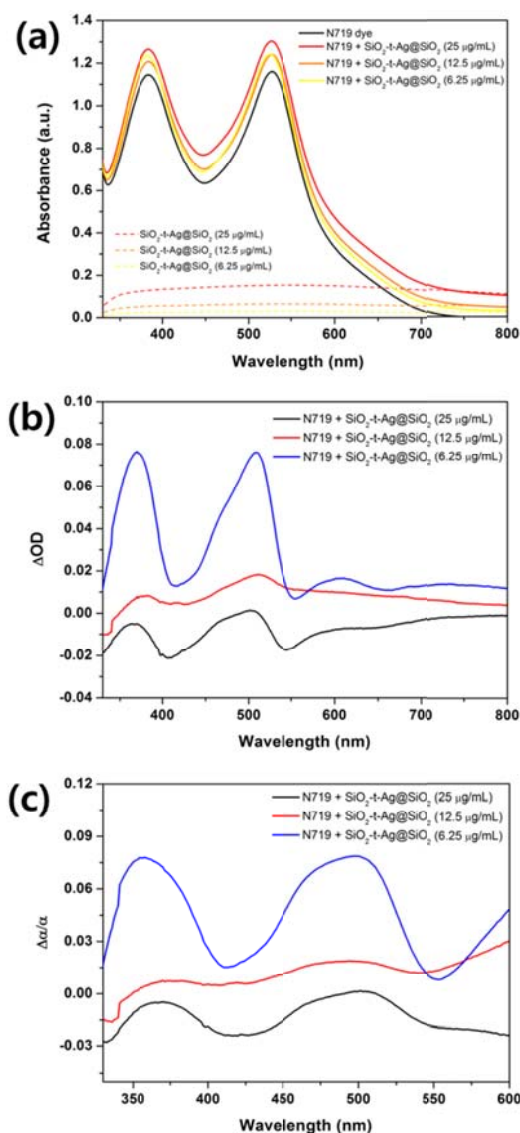
**Figure 3.10 LSPR-induced enhancement of light absorption of dye molecule in solution. (a) UV-vis absorption spectra of N719 dye and SiO₂-t-Ag@SiO₂. (b) Net changes of dye absorption due to the presence of SiO₂-t-Ag@SiO₂. (c) Relative changes of effective extinction coefficient of dye.**

### 3.3.4 UV-Vis absorption and reflectance spectra of photoelectrodes

The optical properties of the photoanodes fabricated using the prepared pastes are shown in Figure 3.11. Generally, photoanode films before and after dye (N719) adsorption showed a similar tendency with the result in solution (Figure 3.10). The UV-vis absorbance of the fabricated photoanodes increased with increasing concentration of $SiO_2$-t-Ag@$SiO_2$ because of the strong plasmon absorption of Ag NPs. To investigate the effects of LSPR from Ag NPs on the optical absorption of N719 dye, the absorbance of pure N719 dye ($Abs_{dye}$) was calculated by subtracting $Abs_{film}$ from $Abs_{film+dye}$. Figure 3.11(b) shows that light absorption by pure dye molecules increased in the presence of $SiO_2$-t-Ag@$SiO_2$. This observation suggested that the increase in UV-vis absorption is mainly due to the LSPR-enhanced light absorption of dye. Diffused reflectance spectra of the photoanodes (Figure 3.11(c)) were not significantly different; however, a slight increase was observed when $SiO_2$-t-Ag@$SiO_2$ or a $SiO_2$ core was incorporated. The increased diffused reflectance of 3 wt% $SiO_2$ indicated that the relatively large size and different refractive index of the $SiO_2$ core could cause a small amount of light scattering. To obtain an optimized performance, paste containing 5 wt% of $SiO_2$-t-Ag@$SiO_2$ was prepared. The photoanode containing 5 wt% of $SiO_2$-t-Ag@$SiO_2$ shows

84

stronger UV-vis absorption because of higher concentration of $SiO_2$-t-$Ag@SiO_2$. (Figure 3.12(c)) However it did not influence light absorption of N719 dye any more. It is mainly due to excessive light absorption by $SiO_2$-t-$Ag@SiO_2$, which is not delivered to the sensitizer completely.
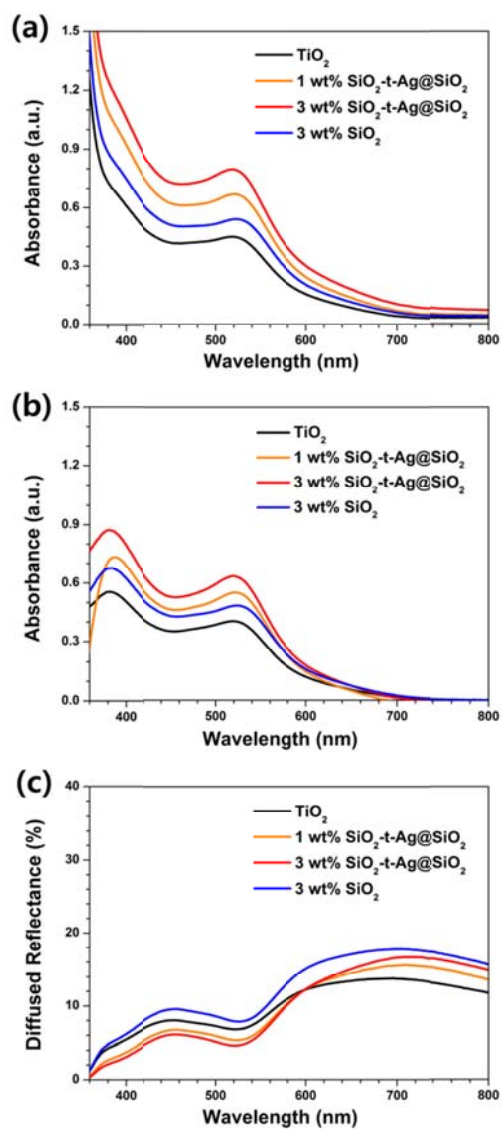
**Figure 3.11 UV-vis absorption spectra of (a) dye-adsorbed photoanodes, (b) pure N719 dyes of photoanodes (Abs$_{film+dye}$ − Abs$_{film}$), (c) diffused reflectance spectra of dye-adsorbed photoanodes.**
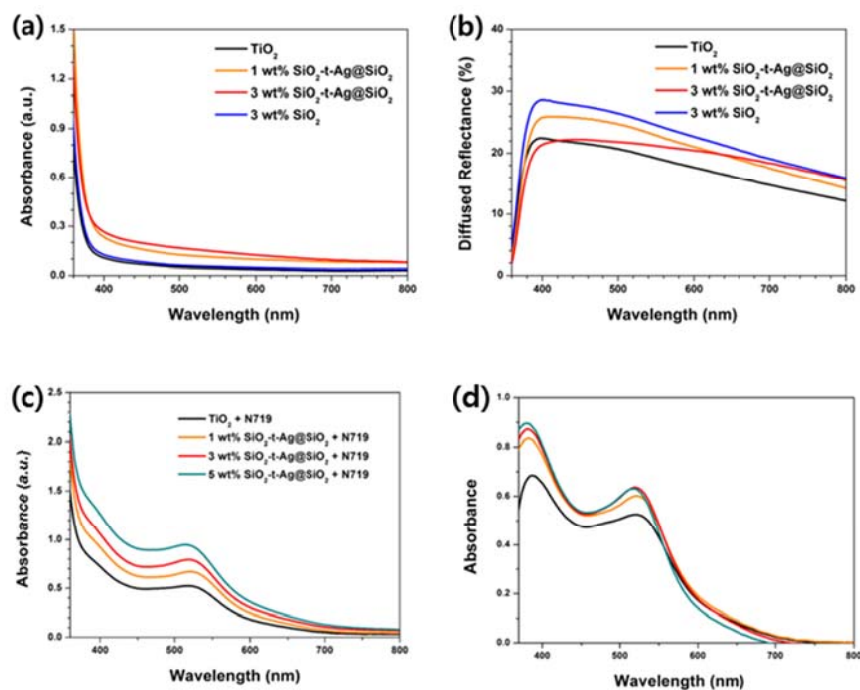
**Figure 3.12 UV-vis absorption spectra of (a) photoanodes before dye-adsorption, (c) dye-adsorbed photoanodes, (d) pure N719 dye in photoanodes (Abs$_{film+dye}$ − Abs$_{film}$). (b) UV-vis diffused reflectance spectra of photoanodes before dye-adsorption.**

### 3.3.5 Photovoltaic characteristics

The photoelectrochemical characteristics of DSSCs with modified photoanodes were examined to confirm the contribution of LSPR to the cell performance. Figure 3.13 shows the current density–voltage ($J$–$V$) characteristics of DSSCs with four types of N719-sensitized photoanodes (TiO$_2$, 1 wt% SiO$_2$-t-Ag@SiO$_2$, 3 wt% SiO$_2$-t-Ag@SiO$_2$, and 3 wt% SiO$_2$), which were measured under simulated sunlight conditions (an intensity of 100 mW/cm$^2$ at AM 1.5G). The main photovoltaic parameters are summarized in Table 3.1. The short-circuit current density ($J_{SC}$), open-circuit voltage ($V_{OC}$), fill factor ($ff$), and power conversion efficiency ($\eta$) of a conventional cell (TiO$_2$ photoanode cell) were 10.08 mA/cm$^2$, 0.76 V, 0.74, and 5.71%, respectively. On the other hand, the same parameters for a 3 wt% SiO$_2$-t-Ag@SiO$_2$ photoanode cell were 12.37 mA/cm$^2$, 0.78 V, 0.73, and 7.05%, respectively. By using SiO$_2$-t-Ag@SiO$_2$, significant improvement (23%) in $J_{SC}$ was observed, and this led to a 23% increase in the power conversion efficiency of the cell as a consequence. The trend of increase in $J_{SC}$ with the concentration of SiO$_2$-t-Ag@SiO$_2$ is clearly shown in Figure 3.13. This increase was mainly due to improved light utilization by LSPR, in agreement with the UV-vis absorption spectroscopy results shown in Figure 3.11(a) and

88

3.11(b). In addition, a slightly higher $J_{SC}$ of 3 wt% $SiO_2$ cell than that of the TiO$_2$ cell showed the existence of additional light scattering by the $SiO_2$ core. These results were well supported by incident photon-to-current efficiency (IPCE) data (Figure 3.14(a)). The IPCEs of the cells coincided with the absorbance spectra of photoanode films across the wavelength region in which the light absorption of N719 was dominant, and this was due to the plasmon-enhanced absorption of N719. For further analysis, we calculated IPCE enhancement factors (Figure 3.14(b)). A steep increase in the 300~400 nm wavelength region was observed for 3 wt% samples, while there was no significant change for the 1 wt% sample in this range. This can be explained by the influence of light scattering. It appears that the light scattering ability increased upon the addition of more $SiO_2$-t-Ag@$SiO_2$ by 2 wt%. The change in $V_{OC}$ was another interesting result, as it increased with the concentration of $SiO_2$. For verification, we also measured $J$–$V$ curves under dark conditions to obtain information about relative recombination rates. As the $SiO_2$ concentration increased, the onset of dark current experienced a shift toward a higher voltage range (Figure 3.13). A large dark current density indicates that the cell had a high recombination rate, and this caused a decrease in $V_{OC}$ by increased back reaction. In the $SiO_2$-blended DSSCs, $SiO_2$ spheres in TiO$_2$ nanostructures could passivate the recombination centers on adjacent TiO$_2$

surfaces, and then suppress electron back-transfer to redox couples in the electrolyte as a consequence. Considering that $SiO_2$ spheres have relatively large size and insulating property, further analysis is required to fully understand the effect of $SiO_2$ spheres on the overall cell system.

To obtain an optimized performance, paste containing 5 wt% of $SiO_2$-t-Ag@$SiO_2$ was prepared. The photoanode containing 5 wt% of $SiO_2$-t-Ag@$SiO_2$ shows stronger UV-vis absorption because of higher concentration of $SiO_2$-t-Ag@$SiO_2$. (Figure 3.15(a)) However, it exhibit lower short-circuit current and power conversion efficiency than 3 wt% cell. (Figure 3.15(b) and 3.15(c)) The short-circuit current density ($J_{SC}$), open-circuit voltage ($V_{OC}$), fill factor (*ff*), and power conversion efficiency ($\eta$) of 5 wt% of $SiO_2$-t-Ag@$SiO_2$ cell were 11.60 mA/cm$^2$, 0.77 V, 0.74, and 6.64%, respectively. It is mainly due to excessive light absorption by $SiO_2$-t-Ag@$SiO_2$, which is not delivered to the sensitizer completely.

DSSCs with ~12 μm $TiO_2$ films were fabricated to investigate the light utilization in thicker semiconductor films. (previous experiments: ~ 6 μm) As shown in Table 3.2 and Figure 3.16, a similar tendency with ~ 6 μm results was verified. Especially, short-circuit current was increased from 14.8 to 16.2 mA/cm$^2$, which was influenced by LSPR. However, the increase (9%) in $J_{SC}$ was smaller than that (23%) in ~ 6 μm results.

**Table 3.1 Photovoltaic parameters of dye-sensitized solar cells**

| Photoanode | $J_{SC}$ (mA/cm$^2$) | $V_{OC}$ (V) | $ff$ | $\eta$ (%) |
|---|---|---|---|---|
| TiO$_2$ | 10.08 ± 0.32 | 0.76 ± 0.02 | 0.74 ± 0.01 | 5.71 ± 0.31 |
| 1 wt% SiO$_2$-t-Ag@SiO$_2$ | 11.26 ± 0.98 | 0.77 ± 0.01 | 0.74 ± 0.02 | 6.40 ± 0.36 |
| 3 wt% SiO$_2$-t-Ag@SiO$_2$ | 12.37 ± 0.98 | 0.78 ± 0.01 | 0.73 ± 0.01 | 7.05 ± 0.53 |
| 3 wt% SiO$_2$ | 10.30 ± 0.60 | 0.78 ± 0.01 | 0.75 ± 0.01 | 6.03 ± 0.35 |
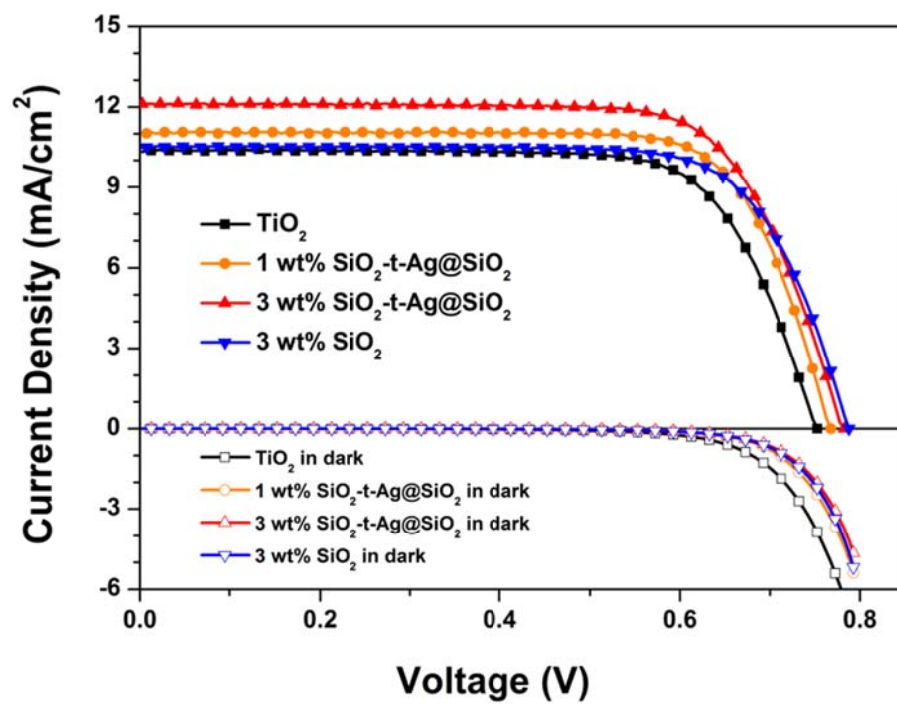
**Figure 3.13 *J–V* curves of DSSCs under illumination and in dark.**
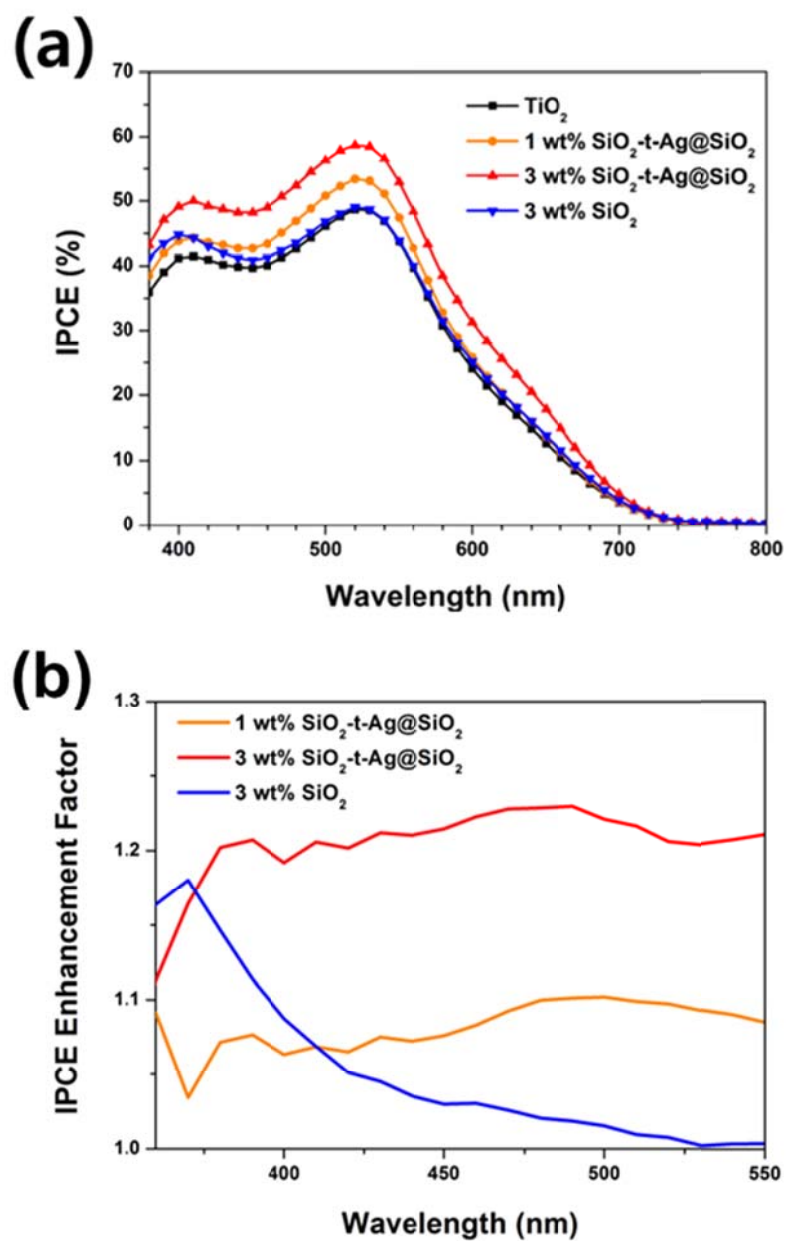
**Figure 3.14(a) Incident photon-to-current efficiency (IPCE) spectra of DSSCs. (b) IPCE enhancement factor (IPCE$_{sample}$/IPCE$_{TiO2}$).**
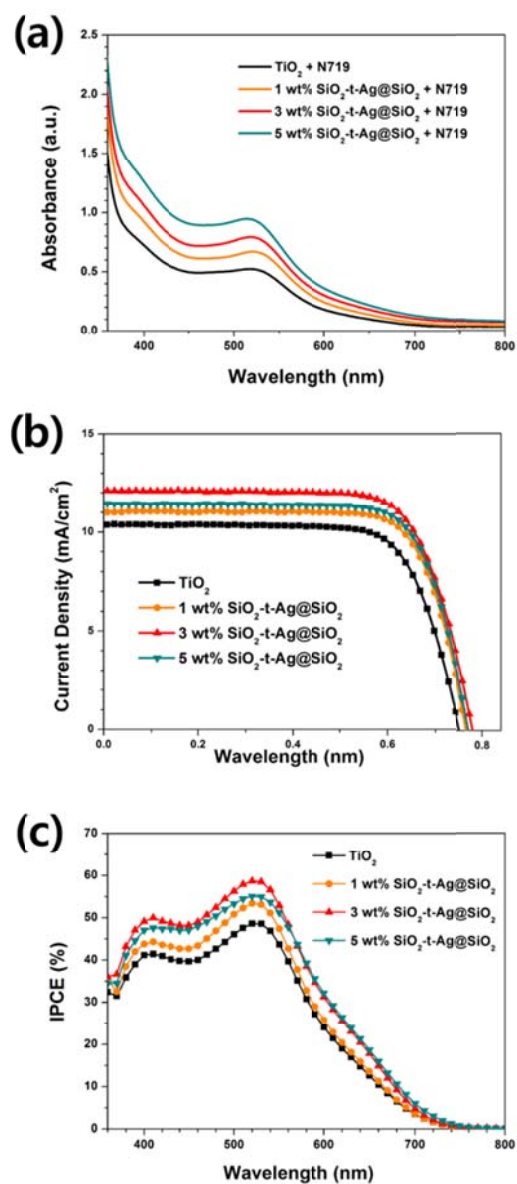
**Figure 3.15(a) UV-vis absorption spectra of photoanodes, (b) *J-V* curves of DSSCs, (c) IPCE spectra of DSSCs.**

**Table 3.2 Photovoltaic parameters of DSSCs with 12 μm photoanodes.**

| Photoanode | $J_{SC}$ (mA/cm$^2$) | $V_{OC}$ (V) | $ff$ | $\eta$ (%) |
|---|---|---|---|---|
| TiO$_2$ (12 μm) | 14.84 | 0.703 | 0.71 | 7.44 |
| 3 wt% SiO$_2$-t-Ag@SiO$_2$ (12 μm) | 16.18 | 0.731 | 0.70 | 8.31 |
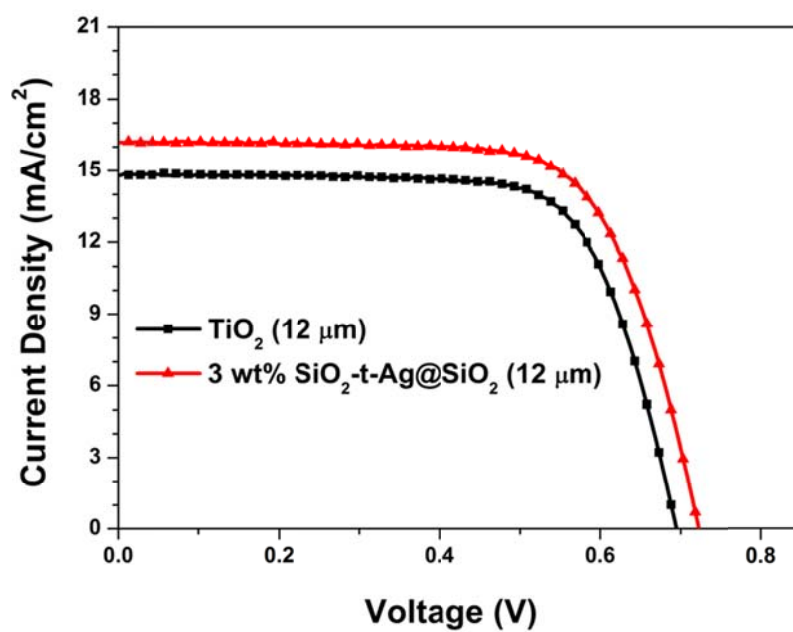
**Figure 3.16** *J-V* curves of DSSCs with 12 μm photoanodes.

### 3.3.6 Absorbed photon-to-current conversion efficiency (APCE)

The absorbed photon-to-current conversion efficiency (APCE) was calculated by dividing measured incident photon-to-current conversion efficiency (IPCE) by light harvesting efficiency (LHE = $1 - 10^{-A}$, with A being the absorbance of the film). APCE spectra of samples are similar because the plasmonic particle does not affect the quantum yield for the electron injection or efficiency of transporting injected electrons, whereas total amount of absorbed photons is affected. At wavelength above 550 nm, APCE of 3 wt% $SiO_2$-t-Ag@$SiO_2$ is lower than that of $TiO_2$, because $SiO_2$-t-Ag@$SiO_2$ absorbs too many photons that do not participate in charge generation. It is due to low far-red light absorption ability of N719.(Figure 1.5) The light trapped by LSPR did not utilize by N179 in longer wavelength region. The high Ag concentration and interparticle interaction between adjacent nanoparticles may result in light to heat conversion by electron−phonon coupling. The dissipation of this heat results in an increase in phonon density, which consequently reduces the number of carriers available for photocurrent generation. [72, 74, 78-80]
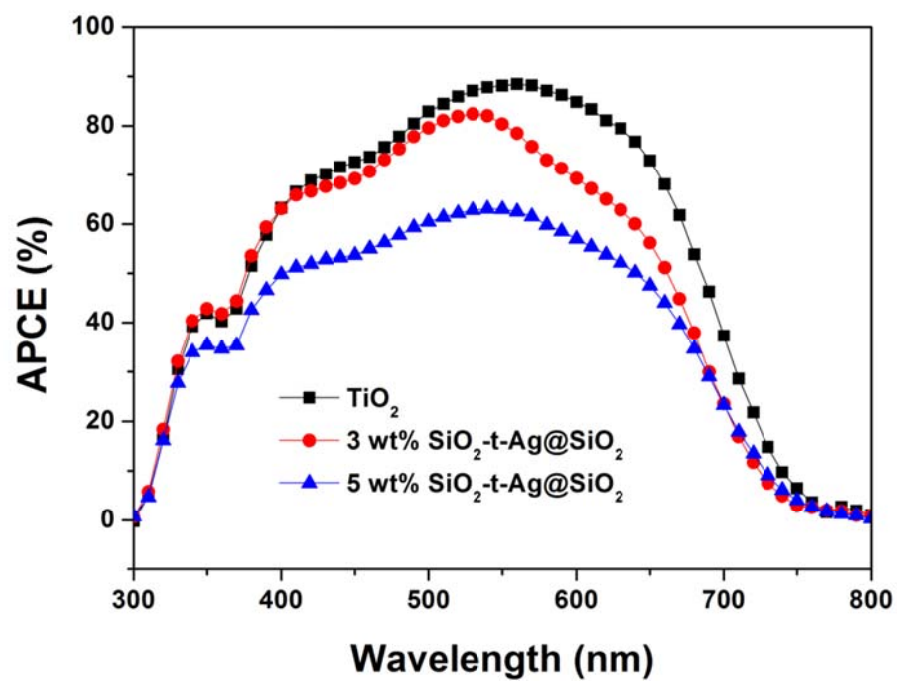
**Figure 3.17 Absorbed photon-to-current conversion efficiency (APCE).**

## 3.4 Conclusions

In summary, the plasmonic enhancement effects of a photoanode in DSSCs were investigated by using $SiO_2$ spheres decorated with tightly assembled silver NPs ($SiO_2$-t-Ag@$SiO_2$). Tightly assembled Ag NPs on a $SiO_2$ core showed broadband plasmonic absorption developed by coupled plasmon modes, which was not limited to a specific wavelength. UV-vis absorption spectra were well corresponded with calculated data. In contrast with $SiO_2$ spheres decorated with sparsely assembled silver nanoparticles ($SiO_2$-s-Ag), $SiO_2$-t-Ag showed broaden and enhanced plasmonic behaviour caused by plasmon coupling. By incorporating $SiO_2$-t-Ag@$SiO_2$ into the photoanodes of DSSCs, light absorption by the photoanode thin films definitely increased. LSPR from $SiO_2$-t-Ag@$SiO_2$ stored the resonance wavelength of light and increased light pathway by plasmonic light scattering. DSSCs with a 3 wt% $SiO_2$-t-Ag@$SiO_2$ photoanode exhibited 20% better power conversion efficiency than a conventional cell, which was mainly due to improved $J_{SC}$ that originated from the plasmon-enhanced light absorption of the photoanode. Using plasmonics to concentrate light, it is expected to reduce the thickness of the photoanode and the amount of N719 dye. If the fabrication process of plasmonic particles is simple and mass-producible, this study can contribute

to commercializing of DSSC, because silver precursor has competitive price in comparison with N719 dye. We also expect that the utilization of this broadband plasmonic behavior produced by tightly assembled silver NPs may bring advances to other fields such as different types of solar cells, Raman spectroscopy, and bioimaging techniques.

# References

[1]. E. Colye, R. A. Simmons, "Understanding the Global Energy Crisis", *Purdue University Press*, Indiana (2014).

[2]. J. Andrews, N. Jelley, "Energy Science", *Oxford University Press*, New York (2007).

[3]. V. Devabhaktuni, M. Alam, S. Depuru, R. C. Green II, D. Nims, C. Near, "Solar energy: Trends and enabling technologies", *Renewable and Sustainable Energy Rev.,* **19**, 555 (2013).

[4]. D. M. Chapin, C. S. Fuller, G. L. Pearson, "A new silicon p-n junction photocell for converting solar radiation into electrical power", *J. Appl. Phys*., **25**, 676 (1954).

[5]. P. Wurfel, "Physics of Solar Cells", *Wiley*, New York (2005).

[6]. M. Grätzel, "Photoelectrochemical cells", *Nature*, **414**, 338 (2001).

[7]. M. Grätzel, "Conversion of sunlight to electric power by nanocrystalline dye-sensitized solar cells", *J. Photochem. Photobiol. A*, **164**, 3 (2004).

[8]. B. O`Regan, M. Grätzel, "Low cost and highly efficient solar cells based on the sensitization of colloidal titanium dioxide", *Nature*, **353**, 737 (1991).

[9]. M. Grätzel, "Solar energy conversion by dye-sensitized photovoltaic cells", *Inorg. Chem.*, **44**, 6841 (2005).

[10]. T. N. Murakami, M. Grätzel, "Counter electrodes for DSC: Application of functional materials as catalysts", *Inorg. Chim. Acta*, **361**, 572 (2008).

[11]. S. Ito, T. N. Murakami, P. Comte, P. Liska, C. Grätzel, M. K. Nazeeruddin, M. Grätzel, "Fabrication of thin film dye sensitized solar cells with solar to electric power conversion efficiency over 10%", *Thin Solid Films*, **516**, 4613 (2008).

[12]. C.-Y. Chen, M. Wang, J.-Y. Li, N. Pootrakulchote, L. Alibabaei, C. Ngoc-le, J. Decoppet, J. Tsai, C. Grätzel, C. Wu, S. M. Zakeeruddin, M. Grätzel, "Highly Efficient Light-Harvesting Ruthenium Sensitizer for Thin-Film Dye-Sensitized Solar Cells", *ACS Nano*, **3**, 3103 (2009).

[13]. L. Han, A. Islam, H. Chen, C. Malapaka, B. Chiranjeevi, S. Zhang, X. Yang, M. Yanagida, "High-efficiency dye-sensitized solar cell with a novel co-adsorbent", *Energy Environ. Sci.*, **5**, 6057 (2012).

[14]. Y. Yen, H. Chou, Y. Chen, C. Hsua, J .T. Lin, "Recent developments in molecule-based organic materials for dye-sensitized solar cells", *J. Mater. Chem.*, **22**, 8734 (2012).

[15]. S. H. Im, H.-j. Kim, J. H. Rhee, C.-S. Lim, S. I. Seok, "Performance

improvement of $Sb_2S_3$-sensitized solar cell by introducing hole buffer layer in cobalt complex electrolyte", *Energy Environ. Sci.*, 4, 2799 (2011).

[16]. R. Plass, S. Pelet, J. Krueger, M. Grätzel, "Quantum Dot Sensitization of Organic−Inorganic Hybrid Solar Cells", *J. Phys. Chem. B*, **106**, 7578 (2002).

[17]. A. Kojima, K. Teshima, Y. Shirai, T. Miyasaka, "Organometal Halide Perovskites as Visible-Light Sensitizers for Photovoltaic Cells", *J. Am. Chem. Soc.*, **131**, 6050 (2009).

[18]. N. J. Jeon, H. G. Lee, Y. C. Kim, J. Seo, J. H. Noh, J. Lee, S. I. Seok, "o-Methoxy Substituents in Spiro-OMeTAD for Efficient Inorganic–Organic Hybrid Perovskite Solar Cells", *J. Am. Chem. Soc.*, **136**, 7837 (2014).

[19]. M. Wang, C. Grätzel, S. M. Zakeeruddin, M. Grätzel, "Recent developments in redox electrolytes for dye-sensitized solar cells", *Energy Environ. Sci.*, 5, 9394 (2012).

[20]. D. Li, D. Qin, M. Deng, Y. Luo, Q. Meng, "Optimization the solid-state electrolytes for dye-sensitized solar cell", *Energy Environ. Sci.*, 2, 283 (2009).

[21]. A. Hagfeldt, G. Boschloo, L. Sun, L. Kloo, H. Pettersson, "Dye-

sensitized solar cells", *Chem. Rev.* **110**, 6595 (2010).

[22]. X. Zhang, J. Zhang, Y. Xia, "A comparative theoretical investigation of ruthenium dyes in dye-sensitized solar cells", *J. Photochem. Photobiol. A*, **185**, 283 (2007).

[23]. E. Dell`Orto, L. Raimondo, A. Sassella, A. Abbotto, "Dye-sensitized solar cells: spectroscopic evaluation of dye loading on TiO$_2$", *J. Mater. Chem.*, **22**, 11364 (2012).

[24]. H.-S. Kim, C.-R. Lee, J.-H. Im, K.-B Lee, T. Moehl, A. Marchioro, S.-J Moon, R. Humphry-Baker, J.-H. Yum, J. E. Moser, M. Grätzel, N.-G. Park, "Lead iodide perovskite sensitized all-solid-state submicron thin film mesoscopic solar cell with efficiency exceeding 9%", *Sci. Rep.*, **2**, 591 (2012).

[25]. A. Yella, H.-W. Lee, H. N. Tsao, C. Yi, A. K. Chandiran, M. K. Nazeeruddin, E. W.-G. Diau, C.-Y. Yeh, S. M. Zakeeruddin, M. Grätzel, "Porphyrin-sensitized solar cells with cobalt (II/III)–based redox electrolyte exceed 12 percent efficiency", *Science*, **334**, 629 (2011).

[26]. H. N. Tsao, C. Yi, T. Moehl, J.-H. Yum, S. M. Zakeeruddin, M. K. Nazeeruddin, M. Grätzel, "Cyclopentadithiophene Bridged Donor–Acceptor Dyes Achieve High Power Conversion Efficiencies in Dye-

Sensitized Solar Cells Based on the tris-Cobalt Bipyridine",
*ChemSusChem*, **4**, 591 (2011).

[27]. S. M. Feldt, E. A. Gibson, E. Gabrielsson, L. Sun, G. Boschloo, A. Hagfeldt, "Design of organic dyes and cobalt polypyridine redox mediators for high-efficiency dye-sensitized solar cells", *J. Am. Chem. Soc.*, **132**, 16714 (2010).

[28]. Y. G. Seo, K. Woo, J. Kim, H. Lee, W. Lee, "Rapid fabrication of an inverse opal $TiO_2$ photoelectrode for DSSC using a binary mixture of $TiO_2$ nanoparticles and polymer microspheres", *Adv. Funct. Mater.*, **21**, 3094 (2011).

[29]. C.-Y. Cho, J. H. Moon, "Hierarchically Porous $TiO_2$ Electrodes Fabricated by Dual Templating Methods for Dye-Sensitized Solar Cells", *Adv. Mater.*, **23**, 2971 (2011).

[30]. S. Hore, P. Nitz, C. Vetter, C. Phahl, M. Niggemann, R. Kern, "Scattering spherical voids in nanocrystalline $TiO_2$–enhancement of efficiency in dye-sensitized solar cells", *Chem. Commun.*, **41**, 2011 (2005).

[31]. M. Adachi, Y. Murata, I. Okada, S. Yoshikawa, "Formation of titania nanotubes and applications for dye-sensitized solar cells", *J. Electrochem. Soc.*, **150**, G488 (2003).

[32]. Y. Ohsaki, N. Masaki, T. Kitamura, Y. Wada, T. Okamoto, T. Sekino, K. Niihara, S. Yanagida, "Dye-sensitized TiO$_2$ nanotube solar cells: fabrication and electronic characterization", *Phys. Chem. Chem. Phys.*, **7**, 4157 (2005).

[33]. M. Kimura, H. Nomoto, N. Masaki, S. Mori, "Dye Molecules for Simple Co-Sensitization Process: Fabrication of Mixed-Dye-Sensitized Solar Cells", *Angew. Chem. Int. Ed.*, **51**, 4371 (2012).

[34]. J. Chang, C.-P. Lee, D. Kumar, P.-W. Chen, L.-Y. Lin, K. R. J. Thomas, K.-C. Ho, "Co-sensitization promoted light harvesting for organic dye-sensitized solar cells using unsymmetrical squaraine dye and novel pyrenoimidazole-based dye", *J. Power Sources*, **240**, 779 (2013).

[35]. K. Shankar, X. Feng, C. A. Grimes, "Enhanced harvesting of red photons in nanowire solar cells: Evidence of resonance energy transfer", *ACS Nano*, **3**, 788 (2009).

[36]. J.-H. Yum, B. E. Hardin, S.-J. Moon, E. Baranoff, F. Nüesch, M. D. McGehee, M. Grätzel, M. K. Nazeeruddin, "Panchromatic Response in Solid-State Dye-Sensitized Solar Cells Containing Phosphorescent Energy Relay Dyes", *Angew. Chem. Int. Ed.*, **48**, 9277 (2009).

[37]. S. Buhbut, S. Itzhakov, E. Tauber, M. Shalom, I. Hod, T. Geiger, Y.

Garini, D. Oron, A. Zaban, "Built-in quantum dot antennas in dye-sensitized solar cells", *ACS Nano*, **4**, 1293 (2010).

[38]. S. Itzhakov, S. Buhbut, E. Tauber, T. Geiger, A. Zaban, D. Oron, "Design Principles of FRET-Based Dye-Sensitized Solar Cells with Buried Quantum Dot Donors", *Adv. Energy Mater.*, **1**, 626 (2011).

[39]. S. Coe, W. K. Woo, M. Bawendi, V. Bulovic, "Electroluminescence from single monolayers of nanocrystals in molecular organic devices", *Nature* **420**, 800 (2002).

[40]. K. W. Johnston, A. G. Pattantyus-Abraham, J. P. Clifford, S. H. Myrskog, D. D. MacNail, L. Levina, E. H. Sargent, "Schottky-quantum dot photovoltaics for efficient infrared power conversion", *Appl. Phys. Lett.* **92**, 151115 (2008).

[41]. M. Schierhorn, S. W. Boettcher, J. H. Peet, E. Matioli, G. C. Bazan, G. D. Stucky, M. Moskovits, "CdSe Nanorods Dominate Photocurrent of Hybrid CdSe− P3HT Photovoltaic Cell", *ACS Nano* **4**, 6132 (2010).

[42]. C. Hu, A. Gassenq, Y. Justo, K. Devloo-Casier, H. Chen, C. Detavernier, Z. Hens, G. Roelkens, "Air-stable short-wave infrared PbS colloidal quantum dot photoconductors passivated with $Al_2O_3$ atomic layer deposition", *Appl. Phys. Lett.*, **105**, 171110 (2014).

[43]. T. P. Osedach, N. Zhao, S. M. Geyer, L. Chang, D. D. Wanger, A. C. Arango, M. C. Bawendi, V. Bulović, "Interfacial Recombination for Fast Operation of a Planar Organic/QD Infrared Photodetector", *Adv. Mater.*, **22**, 5250 (2010).

[44]. M. E. Turk, J. Choi, S. J. Oh, A. T. Fafarman, B. T. Diroll, C. B. Murray, C. R. Kagan, J. M. Kikkawa, "Gate-Induced Carrier Delocalization in Quantum Dot Field Effect Transistors", *Nano Lett*., **14**, 5948 (2014).

[45]. T. Otto, C. Miller, J. Tolentino, Y. Liu, M. Law, D. Yu, "Gate-Dependent Carrier Diffusion Length in Lead Selenide Quantum Dot Field-Effect Transistors", *Nano Lett*., **13**, 3463 (2013).

[46]. I. L. Medintz, A. R. Clapp, H. Mattoussi, E. R. Goldman, B. Fisher, J. M. Mauro, "Self-assembled nanoscale biosensors based on quantum dot FRET donors", *Nat. Mater.,* **2**, 630 (2003).

[47]. A. J. Nozik*,* "Exciton multiplication and relaxation dynamics in quantum dots: applications to ultrahigh-efficiency solar photon conversion", *Inorg. Chem.*, **44**, 6893 (2005).

[48]. R. Vogel, P. Hoyer, H. Weller, "Quantum-sized PbS, CdS, $Ag_2S$, $Sb_2S_3$, and $Bi_2S_3$ particles as sensitizers for various nanoporous wide-bandgap semiconductors", *J. Phys. Chem.,* **98**, 3183 (1994).

[49]. Y. L. Lee, Y. S. Lo, "Highly Efficient Quantum-Dot-Sensitized Solar Cell Based on Co-Sensitization of CdS/CdSe", *Adv. Funct. Mater.*, **19**, 604 (2009).

[50]. Y.-L. Lee, C.-H. Chang, "Efficient polysulfide electrolyte for CdS quantum dot-sensitized solar cells", *J. Power Sources*, **185**, 584 (2008).

[51]. Mora-Sero, S. Gimenez, F. Fabregat-Santiago, R. Gomez, Q. Shen, T. Toyoda, J. Bisquert, "Recombination in quantum dot sensitized solar cells", *Acc. Chem. Res.*, **42**, 1848 (2009).

[52]. D. Gerion, F. Pinaud, S. C. Williams, W. J. Parak, D. Zanchet, S. Weiss, A. P. Alivisatos, "Synthesis and properties of biocompatible water-soluble silica-coated CdSe/ZnS semiconductor quantum dots", *J. Phys. Chem. B,* **105**, 8861 (2001).

[53]. E. I. Altinoglu, J. H. Adair, "Near infrared imaging with nanoparticles", *WIREs Nanomed. Nanobiotechnol.*, **2** , 461 (2010).

[54]. J. Kim, J.E. Lee, J. Lee, J. H. Yu, C. B. Kim, K. An, Y. Hwang, C. H. Shin, J. G. Park, J. Kim, T. Hyeon, "Magnetic fluorescent delivery vehicle using uniform mesoporous silica spheres embedded with monodisperse magnetic and semiconductor nanocrystals", *J. Am. Chem. Soc.* **128**, 688 (2006).

[55]. W. Stöber, A. Fink, "Controlled growth of monodisperse silica spheres in the micron size range", *J. Colloid Interf. Sci.*, **26**, 62 (1968).

[56]. E. A. Jares-Erijman, T. M. Jovin, "FRET imaging", *Nat. Biotechnol.*, **21**, 1387 (2003).

[57]. T. Geiger, S. Kuster, J.-H. Yum, S.-J. Moon, M. K. Nazeeruddin, M. Grätzel, F. Nüesch, "Molecular Design of Unsymmetrical Squaraine Dyes for High Efficiency Conversion of Low Energy Photons into Electrons Using TiO$_2$ Nanocrystalline Films", *Adv. Fucnt. Mater.*, **19**, 2720 (2009).

[58]. A. Bansal, J. S. Sekhon, S. S. Verma, "Scattering Efficiency and LSPR Tunability of Bimetallic Ag, Au, and Cu Nanoparticles", *Plasmonics*, **9**, 143 (2014).

[59]. J. Homola, "Present and future of surface plasmon resonance biosensors", *Anal. Bioanal. Chem.*, **377**, 528 (2003).

[60]. X. Lia, L. Jiang, Q. Zhan, J. Qian, S. He, "Localized surface plasmon resonance (LSPR) of polyelectrolyte-functionalized gold-nanoparticles for bio-sensing", *Colloids and Surfaces A: Physicochemical and Engineering Aspects*, **332**, 172 (2009)

[61]. B.-H. Jun, M. S. Noh, J. Kim, G. Kim, H. Kang, M.-S. Kim, Y.-T. Seo, J. Baek, J.-H. Kim, J. Park, S. Kim, Y.-K. Kim, T. Hyeon, M.-H.

Cho, D. H. Jeong, Y.-S. Lee, "Multifunctional Silver-Embedded Magnetic Nanoparticles as SERS Nanoprobes and Their Applications", *Small*, **6**, 119 (2010).

[62]. H. Kang, S. Jeong, Y. Park, J. Yim, B.-H. Jun, S. Kyeong, J.-K. Yang, G. Kim, S. G. Hong, L. P. Lee, J.-H. Kim, H.-Y. Lee, D. H. Jeong, Y.-S. Lee, "Near-Infrared SERS Nanoprobes with Plasmonic Au/Ag Hollow-Shell Assemblies for In Vivo Multiplex Detection", *Adv. Funct. Mater.*, **23**, 3719 (2013).

[63]. K. Okamoto, I. Niki, A. Shvartser, Y. Narukawa, T. Mukai, A. Scherer, "Surface-plasmon-enhanced light emitters based on InGaN quantum wells", *Nat. Mater.*, **3**, 601 (2004).

[64]. P. Wang, B. Huang, X. Zhang, X. Qin, H. Jin, Y. Dai, Z. Wang, J. Wei, J. Zhan, S. Wang, J. Wang, M.-H. Whangbo, "Highly Efficient Visible-Light Plasmonic Photocatalyst Ag@AgBr" *Chem. Eur. J.*, **15**, 1821 (2009).

[65]. L. Chen, Y. Peng, H. Wang, Z. Gu, C. Duan, "Synthesis of Au@ZIF-8 single- or multi-core–shell structures for photocatalysis", *Chem. Commun.*, **50**, 8651 (2014).

[66]. M. L. de Souza, D. C. Tristão, P. Corio, "Vibrational study of adsorption of Congo red onto $TiO_2$ and the LSPR effect on its

photocatalytic degradation process", *RSC Adv.*, **4**, 23351 (2014).

[67]. X. Zhang, J. Zhao, S. Wang, H. Dai, X. Sun, "Shape-dependent localized surface plasmon enhanced photocatalytic effect of ZnO nanorods decorated with Ag", *Int. J. Hydrogen Energy*, **39**, 8238 (2014).

[68]. H. A. Atwater, A. Polman, "Plasmonics for improved photovoltaic devices", *Nat. Mater.*, **9**, 205 (2010).

[69]. S. D. Standridge, G. C. Schatz, J. T. Hupp, "Distance dependence of plasmon-enhanced photocurrent in dye-sensitized solar cells", *J. Am. Chem. Soc.*, **131**, 8407 (2009).

[70]. M. D. Brown, T. Sureewong, R. S. S. Kumar, V. D'Innocenzo, A. Petrozza, M. M. Lee, U. Wiesner, H. J. Snaith, "Plasmonic Dye-Sensitized Solar Cells Using Core−Shell Metal−Insulator Nanoparticles", *Nano Lett.*, **11**, 438 (2011).

[71]. C. Nahm, H. Choi, J. Kim, D.-R. Jung, C. Kim, J. Moon, B. Lee, B. Park, "The effects of 100 nm-diameter Au nanoparticles on dye-sensitized solar cells", *Appl. Phys. Lett.*, **99**, 253107 (2011).

[72]. J. Qi, X. Dang, P. T. Hammond, A. M. Belcher, "Highly efficient plasmon-enhanced dye-sensitized solar cells through metal@oxide core–shell nanostructure" *ACS Nano*, **5**, 7108 (2011).

[73]. N. C. Jeong, C. Prasittichai, J. T. Hupp, "Photocurrent enhancement by surface plasmon resonance of silver nanoparticles in highly porous dye-sensitized solar cells", *Langmuir*, **27**, 14609 (2011).

[74]. S. Chang, Q. Li, X. Xiao, K. Y. Wong, T. Chen, "Enhancement of low energy sunlight harvesting in dye-sensitized solar cells using plasmonic gold nanorods", *Energy Environ. Sci.*, **5**, 9444 (2012).

[75]. C. Sönnichsen, B. M. Reinhard, J. Liphardt, A. P. Alivisatos, "A molecular ruler based on plasmon coupling of single gold and silver nanoparticles", *Nat. Biotechnol.*, **23**, 741 (2005).

[76]. S. Lin, M. Li, E. Dujardin, C. Girard, S. Mann, "One-Dimensional Plasmon Coupling by Facile Self-Assembly of Gold Nanoparticles into Branched Chain Networks", *Adv. Mater.*, **17**, 2553 (2005).

[77]. S. W. Sheehan, H. Noh, G. W. Brudvig, H. Cao, C. A. Schmuttenmaer, "Plasmonic enhancement of dye-sensitized solar cells using core–shell–shell nanostructures", *J. Phys. Chem. C*, **117**, 927 (2013).

[78]. S. H. Hwang, D. H. Shin, J. Yun, C. Kim, M. Choi, J. Jang, "SiO$_2$/TiO$_2$ Hollow Nanoparticles Decorated with Ag Nanoparticles: Enhanced Visible Light Absorption and Improved Light Scattering in Dye-Sensitized Solar Cells", *Chem. Eur. J.*, **20**, 4439 (2014).

113

[79]. X. Dang, J. Qi, M. T. Klug, P.-Y. Chen, D. S. Yun, N. X. Fang, P. T. Hammond, A. M. Belcher, "Tunable Localized Surface Plasmon-Enabled Broadband Light-Harvesting Enhancement for High-Efficiency Panchromatic Dye-Sensitized Solar Cells", *Nano Lett.*, **13**, 637 (2013).

[80]. X. Zhang, Y. L. Chen, R.-S. Liu, D. P. Tsai, "Plasmonic photocatalyst", *Rep. Prog. Phys.*, **76**, 046401 (2013).

# 국문초록

## 염료감응형 태양전지를 위한 향상된
## 빛의 활용성을 가진 광전극 제조

최정우

서울대학교

공과대학 화학생물공학부

지구 전체의 에너지 소비량 증가와 환경적인 문제, 그리고 화석 연료의 유한함 때문에 신재생에너지 개발에 대한 관심이 높아지고 있다. 그 중에서 태양에너지는 특별한 공해를 만들지 않고, 무한한 에너지를 기반으로 하기 때문에 많은 주목을 받고 있다. 염료감응형 태양전지는 값싸고 쉬운 제조 공정과 심미적인 디자인으로 만들 수 있다는 장점을 지닌 새로운 형태의 태양전지이다. 하지만 염료감응형 태양전지로 기존의 실리콘 기반의 태양전지를 대체하기 위해서는 전체적인 광전환 효율을 더 증가시켜야만 한다. 염료감응형 태양전지의 효율을 높이기 위해서는 가장 중요한 구성요소인 광전극에서의 빛 흡수를 증가시켜서 더 많은 광전자를

발생시켜야한다. 그래서 기존의 많은 연구자들은 광전극에서의 빛 흡수율을 높이기 위해서 많은 노력들을 해왔다. 더 넓은 파장의 빛을 흡수하고, 더 높은 흡광계수를 가지는 새로운 감광제를 개발하거나, 빛의 산란을 이용할 수 있는 새로운 구조의 반도체 전극을 제조하거나, 기존의 염료들을 섞어서 함께 사용하거나, 새로운 개념의 에너지 전달방법을 도입하는 등의 연구를 통해서 광전극의 빛의 효율을 높이는 연구를 진행해왔다. 그럼에도 불구하고 아직 원하는 수준의 빛의 효율을 얻기에는 어려움이 있다. 그래서 본 연구에서는 빛에 반응하는 무기 소재, 양자점이나 금속 나노물질을 염료감응형 태양전지의 광전극에 도입함으로써, 광전극 내에서의 빛의 활용도를 증가시키고자 한다.

연구의 첫 번째 부분에서는 실리카로 코팅된 양자점을 이용해서 빛을 가둬두는 연구를 진행했다. 양자점은 강한 빛 흡수와 방출 능력 때문에 태양전지에 적용될 수 있는 좋은 물질로 평가받고 있다. 하지만 요오드 전해질 내에서의 불안정성 때문에 양자점을 염료감응형 태양전지에 적용할 수 없었다. 본 연구에서는 많은 수의 양자점을 실리카에 붙이고, 다시 실리카로 양자점을 코팅하는 방법을 사용하여, 전해질 속에서도 안정한 $SiO_2/QD@SiO_2$ 를 만들었다. $SiO_2/QD@SiO_2$ 가 도입된 광전극을 가지는 염료감응형 태양전지는 향상된 빛의 이용을 통해 높은

단락전류를 보였고, 이는 향상된 성능에 기여했다. 양자점은 염료감응형 태양전지 내에서 감광제의 역할을 수행하지 않고, 빛을 흡수해서 재방출하는 역할을 수행하였다.

연구의 두 번째 부분은 플라즈몬에 의해 향상된 염료감응형 태양전지의 제조에 관한 것이다. 이 부분에서는 플라즈몬 증폭 현상이 염료감응형 태양전지에 어떤 영향을 미치는지에 대해 분석되었다. 특별히 물질 내에서 플라즈몬간의 결합 (plasmon coupling) 을 유도하기 위해서, 전자기파 시뮬레이션을 통한 새로운 구조의 은 나노물질 결합체 (SiO$_2$-t-Ag@SiO$_2$) 를 디자인했다. 하나의 코어에 은 나노물질을 빽빽하게 도입함으로써, 플라즈몬간의 결합을 유도했고, 이는 하나의 특정 파장이 아닌 넓은 파장 영역에 걸친 강한 빛의 흡수를 가능하게 했다. SiO$_2$-t-Ag@SiO$_2$를 광전극에 도입하여 광전극 위에 흡착된 염료의 흡광 단면을 증가시켰고, 이는 전체 광전극 필름의 흡광계수를 증가시켰다. 국부적 표면 플라즈몬에 의해서 향상된 빛의 흡수는 더 높은 광전류를 생성하도록 했으며, 이는 전체적인 성능 향상에 기여하였다.